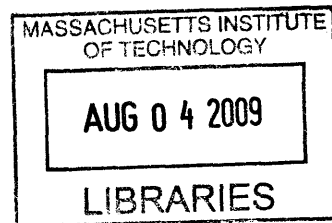# STM Studies of the Nanoscale Electronic Landscape of the Cuprates

by

William Douglas Wise

B.A. Physics
B.A. Materials Science and Mechanical Engineering
Harvard University, 2002

SUBMITTED TO THE DEPARTMENT OF PHYSICS IN PARTIAL
FULFILLMENT OF THE REQUIREMENTS FOR THE DEGREE OF

DOCTOR OF PHILOSOPHY IN PHYSICS
AT THE
MASSACHUSETTS INSTITUTE OF TECHNOLOGY

SEPTEMBER 2009

ARCHIVES

Signature of Author: _

Department of Physics
June 19, 2008

Certified by: _____

Eric W. Hudson
Associate Professor
Thesis Supervisor

Accepted by: _____

Thomas J. Greytak
Professor, Associate Department Head for Education

1

STM Studies of the Nanoscale Electronic Landscape of the Cuprates

by

William Douglas Wise

ABSTRACT

Scanning tunneling microscopy (STM) studies of the high-T_c superconductors have led to a number of important discoveries. In particular, STM has revealed spatial patterns in electronic density due to phenomena such as checkerboard order and quasiparticle interference.

This thesis presents two studies of these patterns and their implications. In the first, I present a doping and temperature dependent study of checkerboard order in the cuprate superconductor $Bi_2Sr_2CuO_{6+x}$ (Bi-2201). The main result, that the wavelength of checkerboard order increases with doping and is independent of temperature, is consistent with a charge density wave origin of the checkerboard and is inconsistent with many other theories.

The second study examines local properties of checkerboard order and of quasiparticle interference patterns in Bi-2201 and the related superconductor $Bi_2Sr_2CaCu_2O_{8+x}$ (Bi-2212). Both of these phenomena are tied to the doping of the material via the configuration of the Fermi surface. I find local variation in both checkerboard order wavelength and in the quasiparticle interference patterns. These variations are consistent with local variations in Fermi surface properties. The discovery of local variations in Fermi surface provides a new way of thinking about other inhomogeneous properties of the cuprates and of inhomogeneous materials in general.

Thesis Supervisor: Eric W. Hudson
Title: Associate Professor of Physics

3

Table of contents

Table of figures

How to use this thesis

"Speak English! I don't know the meaning of half those long words, and I don't believe you do either!"
—Eaglet, Alice in Wonderland

"It looked insanely complicated, and this was one of the reasons why the snug plastic cover it fitted into had the words DON'T PANIC printed on it in large friendly letters."
—The Hitchhiker's Guide to the Galaxy

A friend told me that the average thesis is read a total of 1.8 times, including readings by the author, the review committee, the author's family, friends, and significant other, and other graduate students in the field. While this is somewhat tongue-in-cheek, it gets at the essential truth that a thesis is a huge body of work, and only small parts are going to be important, interesting, and comprehensible to any given audience. In this section, I attempt to make skipping large chunks of thesis as convenient as possible for the reader.

Chapter 1 is an introduction to the physics of this thesis. Most of it should be accessible to the interested reader who knows little physics. People who may find it useful or interesting include friends and family, undergraduates, and beginning graduate students, but most of it can be skipped by practicing physicists and by the review committee.

Chapter 2 is very heavily based on my publication on the doping and temperature dependence of checkerboard order in the cuprate superconductor Bi-2201.[1] Chapter 3, similarly, is very heavily based on a second paper on variations in the cuprate Fermi surface.[2] The first section of each chapter is an attempt to explain the results in terms understandable to non-specialists. The rest of these chapters is more technical. Neither of these chapters is at all accessible to non-physicists, although some of the pictures are pretty (though to be honest, most are not). I imagine these chapters may be read by new graduate students and by the review committee.

For the reader's convenience, I have starred sections based on their prerequisites. No stars implies that the section requires minimal background and can be read by almost anyone. One star means that an undergraduate-level physics education is required for full understanding: usually this means that undergraduate level quantum mechanics or statistical mechanics is assumed. Two stars implies an understanding of solid state physics is required, at the level of a standard introductory course. A section with three stars will probably be understandable only to practitioners of the field.

1.0   Conceptual background

This first and longest chapter discusses background information needed to understand the original research contained in this thesis.

Section 1.1 introduces scanning tunneling microscopy, which is the experimental technique I used to obtain the data. Sections 1.2 and 1.3 are more scientific, and discuss superconductivity and some basic solid state physics concepts. Section 1.2 focuses on so-called "conventional" superconductivity, which is generally well-understood. Section 1.3 discusses properties of the unconventional, "cuprate" superconductors, which are not well-understood. The research of chapters 2 and 3 was done on the cuprates.

1.10 Imaging atoms with a scanning tunneling microscope

Almost all of the work for this thesis involved a scanning tunneling microscope (STM). STM is a powerful tool for studying surfaces at the atomic scale. In many materials, STM can easily image individual atoms. One of the most famous images in science is that of the word IBM spelled out in single xenon atoms by IBM scientists,[3] which dramatically demonstrates both the imaging and manipulation capabilities of the STM.
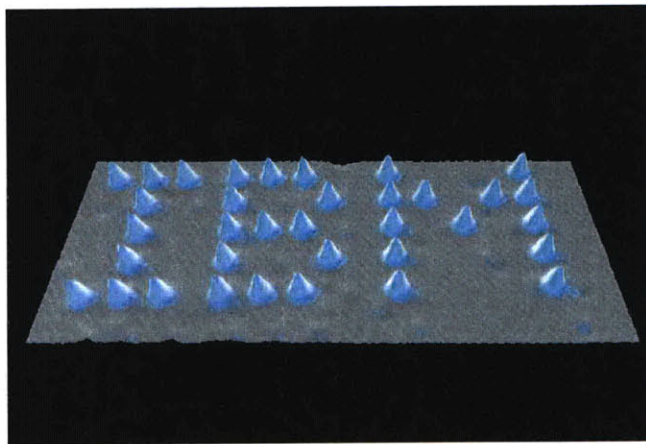
Figure 1. Xenon atoms arranged on a flat nickel surface.
Individual atoms can be moved and imaged by a scanning tunneling microscope.

An STM works by bringing a sharp piece of electrically conducting material (the "tip") very near the surface under observation (the "sample"). Tip materials and preparation techniques vary widely between groups. Our experiments use mechanically cut platinum-iridium alloy wire.

The tip and sample are maintained at different voltages. When the tip and sample are very close, but not quite touching (separation of roughly one atomic diameter) then electrons can jump across the gap separating them, creating an electrical current. The

strength of this current is sensitive to the distance between the tip and sample, to the tip's position on the sample surface, to the voltage applied, and to the surface properties. In STM measurements, one or more of these parameters is varied, and information about the sample is gained by studying the resulting change in current.
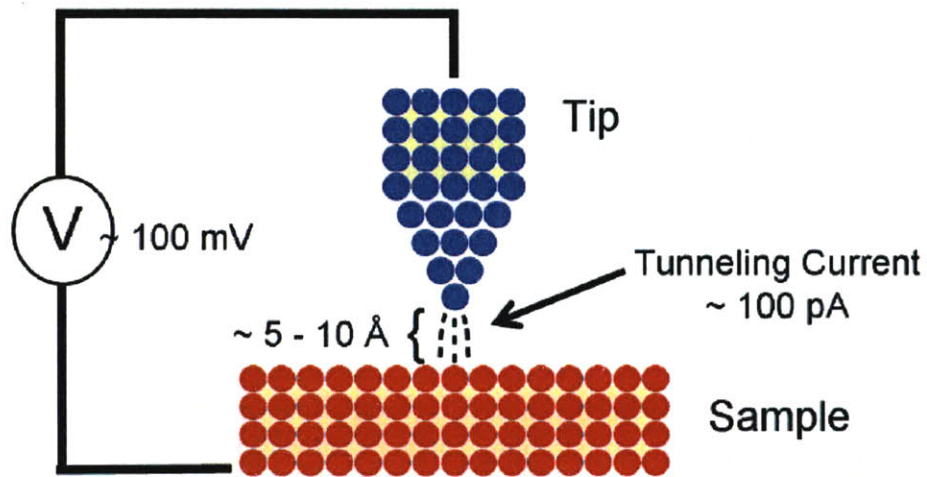
Figure 2. The tip-sample interface.[4]
A voltage difference (in our work, usually ~100 mV) is applied between a tip and sample that are separated by a few atomic diameters. The voltage changes their relative potential, causing electrons to tunnel into areas where they have lower potential energy. Measurements of this flow of electrons form the basis of scanning tunneling microscopy.

There are three standard STM measurement modes that I will discuss here. The first, and most intuitive, is constant current scanning or topographic scanning. In these measurements, the tip voltage is held constant. The tip scans back and forth across the sample surface, and variation in the surface height require the tip be moved vertically in order to maintain constant current. In this way, surface height as a function of position is encoded in the tip height's variation with position. Measurements of tip height are taken in a dense grid across the sample, giving a map of surface height, which is viewed as a two-dimensional image. Maps of surface height taken in this way are generally referred to as topographies or topographic scans. The picture of the atoms arranged form the word IBM is an example of a topography. The images shown in figure Figure 3 are also topographic scans showing individual atoms.
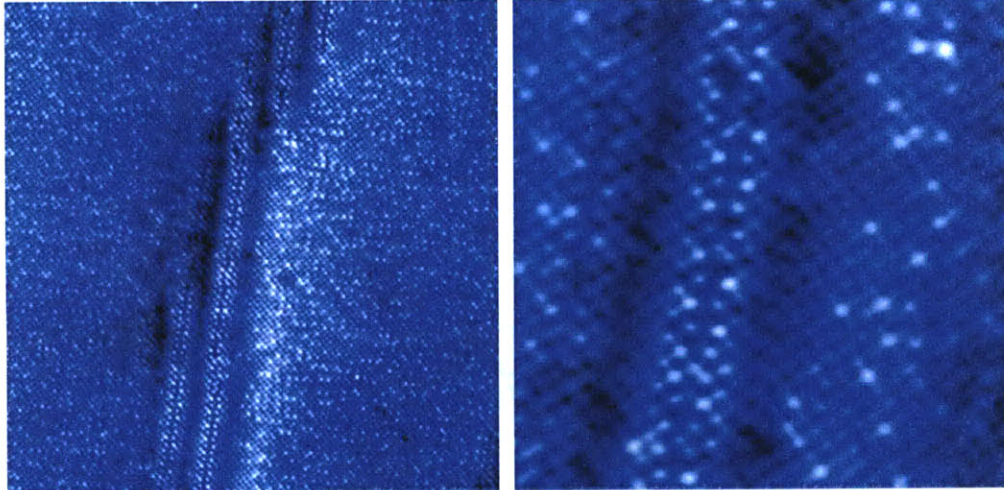
Figure 3. Topography of the superconductor Bi-2201.
These are 400Å square (left) and 100Å square (right) images of the cuprate superconductor called Bi-2201. (The Å is a unit of length equaling 10^{-10} meters.) Most atoms visible are bismuth atoms. Bright atoms are lead. This is a height map, with bright parts of the surface being higher. Thus, this is not a true "image:" the color is meaningless and blue was chosen for cosmetic reasons.

The second common mode involves holding tip position constant and changing the voltage, measuring how the current changes in response to changes in voltage. This gives information about a very important quantity called the local density of states, which describes the energy distribution of states available for electrons to occupy at a given position in the sample. This will be discussed in more detail in the next section. We call data taken in this way "spectroscopy" or a "dI/dV curve" and the resulting data is viewed as a one-dimensional graph (e.g. Figure 4). Much of this thesis depends on studying variations in spectroscopy as a function of position.
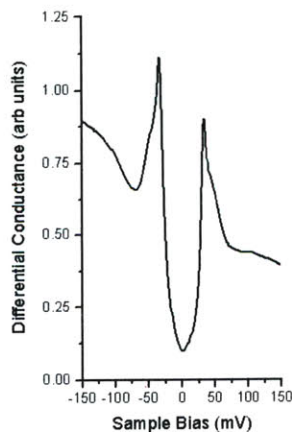
Figure 4. Typical spectroscopy of the superconductor Bi-2212.

The final mode is referred to as "spectral surveys," "dI/dV maps," or "DOS maps," and it combines the previous two modes of measurement. In a spectral survey, spectroscopy is taken at every point on a spatial grid. Topography is generally taken on these grid points at the same time. In this way, every pixel in a two-dimensional image is

9

associated with a one-dimensional dI/dV curve, creating a three-dimensional dataset. This data can be viewed in several ways. One common way to view these is a "conductance map" which looks at maps the value of dI/dV curves at a given voltage as a function of position. This creates a 2D image, such as that of Figure 5.
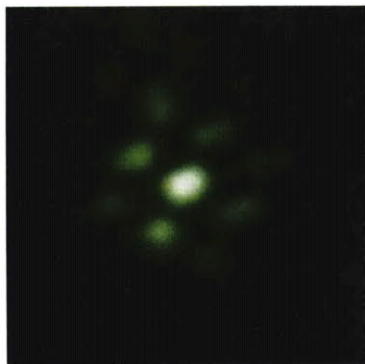
Figure 5. Conductance map of Bi-2201.[5]
The image shown here shows the effect of an impurity on its environment. The local density of states is much higher in the region around the impurity at some energies (here, -2 mV).

There are numerous practical experimental difficulties in the implementation of a STM. One is that the currents being measured are very small, requiring that the electronic system be very sensitive to small signals while free of extraneous noise. Another is that, since individual atoms are typically observed, environmental vibrations must be kept to an extremely low level—a displacement of the tip by a tenth of an atomic diameter is quite noticeable. This can be a difficult requirement to meet in an urban environment. The control, feedback, and data acquisition systems are complex and difficult to implement. In addition to these general difficulties, some studies impose additional requirements. Our experiments, for example, require cryogenic temperatures (~4K, or -269 degrees C) and ultra-high vacuum levels (~10^{-11} atmospheres).
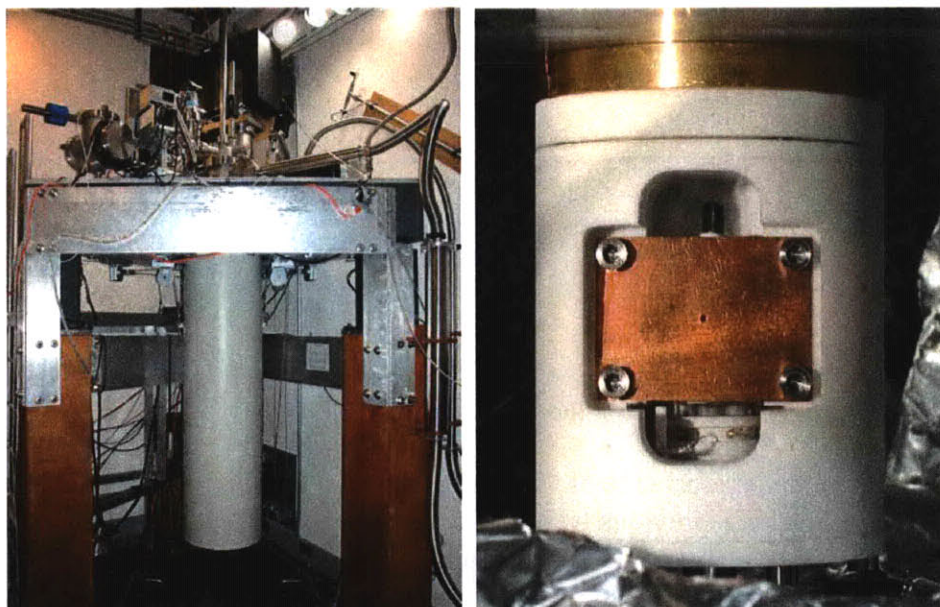
Figure 6. Experimental setup (left) and close-up view of STM (right).

1.11 Scanning tunneling microscopy—theory *

The mechanism controlling current flow from tip to sample, or vice versa, is in general quite complex. Here, I present a simple model based on elementary quantum mechanics. Using insights from this model, I will revisit the measurement modes discussed in the previous section.

The system consisting of the metallic STM tip, the sample, and a junction separating them can be modeled as a square-wave barrier (the junction) separating two lower-potential regions (the tip and sample). The height of this barrier, ϕ, is referred to as the work function and is the energy needed to eject an electron into the vacuum. This is typically of order ~4 eV, though it varies by material.

The tip and sample are thought of as separate systems with their own local density of states (LDOS). There is some overlap between the two systems through the finite barrier. The tip is a virtual ground. Some electrons tunnel from the tip into the sample across the vacuum barrier, and vice versa. When the tip and sample are at the same voltage, these two currents cancel. Negative voltage applied to the sample has the effect of raising the energy of electrons there, increasing the rate of tunneling of electrons from sample to tip through the potential barrier, while decreasing the tunneling rate from tip to sample, leading to a net current. Positive voltage has the opposite effect. It is this current which is what is measured by STM.

For elastic tunneling, which is the dominant process in most STM, electrons will flow out of filled states and into empty states. The tunneling current from sample to tip at a given energy ε is:

$$I_{s \to t, \varepsilon} = -\frac{4\pi e}{\hbar} |M|^2 \, LDOS_s(\varepsilon + eV)(1 - f(\varepsilon + eV)) * LDOS_t(\varepsilon)(f(\varepsilon))$$

A similar equation describes the current in the opposite direction. $LDOS_s$ and $LDOS_t$ are the local densities of states of the sample and tip respectively, and $f(\varepsilon)$ is the Fermi-Dirac distribution function, which takes into account finite-temperature effects.

M is the tunneling matrix element: it contains information about the tip sample junction—most importantly, the tip-sample separation. M is typically not fully known in STM, but we can estimate some of its properties, most importantly, the dependence of M on tip-sample separation. We use the WKB approximation for tunneling through a square barrier: in general, for electrons of mass m tunneling through a barrier with height V_0 and width z, the tunneling matrix element will be given by:

$$|M|^2 = e^{-2\gamma}$$

$$\gamma = \frac{z}{\hbar}\sqrt{2mV_0}$$

In STM, V_0 represents the work function and z represents the tip-sample separation. This implies that the current decays exponentially with increasing tip-sample separation. Empirically, this is the case when tip quality is good. A high work function implies high tip sensitivity.

The total current is the sum of this tunneling current over all energies and both directions:

$$I = -\frac{4\pi e}{\hbar} \int |M|^2 LDOS_s(\varepsilon + eV) LDOS_t(\varepsilon)[f(\varepsilon)(1 - f(\varepsilon + eV)) - (1 - f(\varepsilon))f(e + eV)]d\varepsilon$$
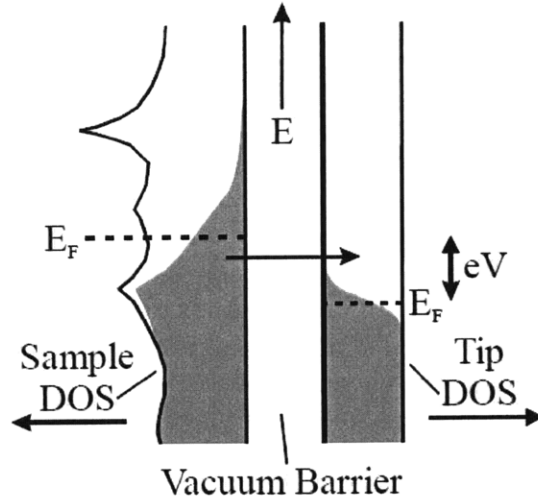
Figure 7. Quantum mechanical tunneling between materials of differing DOS.[6]
A bias voltage V is applied between the tip and sample. This voltage changes the energies of the electrons in the materials, shifting their relative Fermi energies by eV. Electrons reduce their energy by tunneling to the material with the lower Fermi energy (whether this is the tip of sample depends on the sign of the bias voltage). In this picture, solid lines represent the density of allowed states, and the shaded area represents the density of actually filled states. These do not exactly correspond because, at finite temperature, some low-energy states go unoccupied due to thermal excitation.

This equation is often simplified. First, as shown, the tip is usually chosen so that its DOS is flat. We use PtIr tips, sharpened by field emission against gold. All tips are checked for flat density of states against gold targets before being used to gather data. To the extent that the tip DOS is flat over the energy range of interest, we can consider $LDOS_t$ a constant and remove it from the integral.

Second, in the low temperature limit, the Fermi-Dirac distribution $f(\varepsilon)$ is a step function with value 1 below the Fermi energy and 0 above it. We often (though not always![4,7]) work at temperatures where approximating $f(\varepsilon)$ as a step function is valid. If this holds, then the integral is zero below for energies below –eV or above 0.

With these approximations, the tunneling current is given by

$$I = \frac{4\pi e}{\hbar} e^{-2z\sqrt{2mV_0}/\hbar} LDOS_t \int_{-eV}^{0} LDOS_s(\varepsilon)d\varepsilon$$

More important is the *derivative* of I with respect to bias voltage V:

$$dI/dV(\varepsilon) = \left(\frac{4\pi e}{\hbar} e^{-2z\sqrt{2mV_0}/\hbar} LDOS_t \right) LDOS_s(\varepsilon)$$

$$dI/dV(\varepsilon) = I_0 * LDOS_s(\varepsilon)$$

In this equation, I_0 is constant. So, at low temperatures and for a tip with flat density of states, the derivative of current with respect to bias voltage is proportional to the density of states. Almost all interpretations of STM results are based on this result.

We are now in a position to revisit our discussion of STM measurements from the previous section.

One important point is that the current always depends on *both* the LDOS of the sample and the tip-sample separation z. It is therefore impossible to tell if variations in current at different points in the sample are due to variations in height or due to changes in the LDOS. Because of this, topographic images must be interpreted with care. Consider for example the following image.
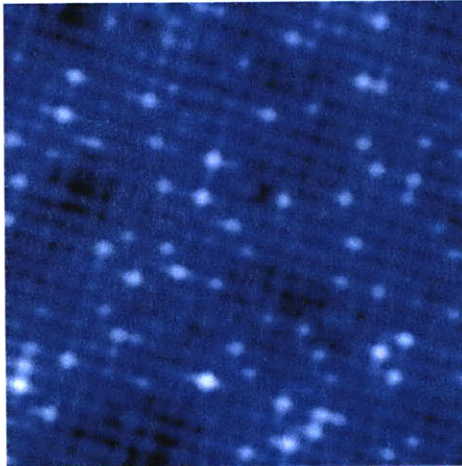
Figure 8. Topographic scan (90Å) of Pb-doped Bi-2201.

In this image (as in almost all topographic images), brightness represents the height to which the tip must be brought in order to maintain some constant current I_0. The regular square atomic lattice is apparent. There are bright and dark areas overlaid on the lattice. These areas may consist of atoms that are physically higher or lower, or may consist of areas with excess or depleted density of states. Further, there are isolated, especially bright, atoms. Their brightness may consist of them being of larger size or may reflect a difference in the density of states here. Based on the information in this image alone, there is no way to distinguish between these possibilities.

As shown earlier, the derivative of current with respect to voltage is proportional to the LDOS, at zero temperature. Spectroscopy taken in this way are the most important measurements taken by STM. Such measurements can in principle be taken by differentiating $I(V)$ curves: however, numerical differentiation in general is a noisy process. More typically, we measure the derivative directly using a lock-in technique. To find the derivative at some voltage V, we set the voltage to V and then add a modulation $V_1*\sin(\omega t)$ where V_1 is small compared to the voltage scale on which the derivative varies

13

(i.e. $I(V)$ is approximately linear from $V-V_1$ to $V+V_1$). This leads to a sinusoidal modulation of the current. The magnitude of this current modulation is proportional to dI/dV, and can be measured very accurately by a lock-in amplifier. (The tip height is held constant throughout this process.) There are tradeoffs in selecting the value of V_1: high V_1 implies a strong, easily measured signal, but fine details of the LDOS can be smoothed over and lost if they occur on an energy scale smaller than eV_1. Small V_1 improves energy resolution, but may require long averaging times in order to obtain good signal-to-noise ratios. In practice, smoothing from V_1 is often the limit on the resolution of STM measurements.

The other limit on spectroscopic resolution comes from finite-temperature effects. Earlier, we approximated the Fermi-Dirac distribution function as a step function when finding that the current was proportional to the LDOS. This is only true at zero temperature: at finite temperature, the Fermi-Dirac distribution goes from 1 to 0 over an energy range of order kT. This results in smoothing of the observed LDOS over an energy window of width of a few kT. At 4 K, $kT\sim0.36$ mV, which is small compared to most features of interest—the lock-in effects the described earlier dominate thermal broadening at these temperatures. However, this thermal smoothing becomes important at higher temperatures.

1.20 Conventional superconductivity

Electrical current consists of the flow of charge within a material. In most materials, charge is carried by electrons. As electrons move through the material, they occasionally collide with atoms, with defects in the material, or with each other. In these collisions, the electrons lose energy, which ultimately turns into heat. Thus it takes continual input of energy to drive electrical current, in order to compensate for the constant loss of energy to the so-called *resistance* of the material. The energy lost to resistance ends up heating the material. Both the energy loss and the heating are usually undesirable effects—the energy lost is unavailable to do useful work, and the heating can cause damage.

Superconductivity is a technologically and scientifically important phenomenon in which some materials, when cooled below some material-specific critical temperature T_c, allow electrical current to flow without resistance. Thus current can flow essentially forever without losing any energy or creating any heat, or can be transmitted over large distances without loss. This is possible because in superconductors electrons form pairs, known as Cooper pairs, in which electrons move together. These pairs are not easily scattered by the material and therefore can transport charge without resistance. In most materials, the details of this mechanism are described by so-called BCS theory, after Bardeen, Cooper, and Schrieffer who jointly developed it in 1957.[8-10]

The other fundamental property of superconductors is that they expel magnetic fields, an effect called the Meissner effect. The surface of a superconductor below T_c is a nearly perfect barrier to low-strength magnetic fields: surface currents configure themselves in such a way as to cancel incoming fields. If a superconductor encounters a high-strength field, this perfect cancellation breaks down; in so-called Type I superconductors, superconductivity is destroyed at a critical field H_c, whereas in Type II superconductors, magnetic field begins to penetrate the material at H_{c1}, but superconductivity is not destroyed until a higher critical temperature H_{c2}.
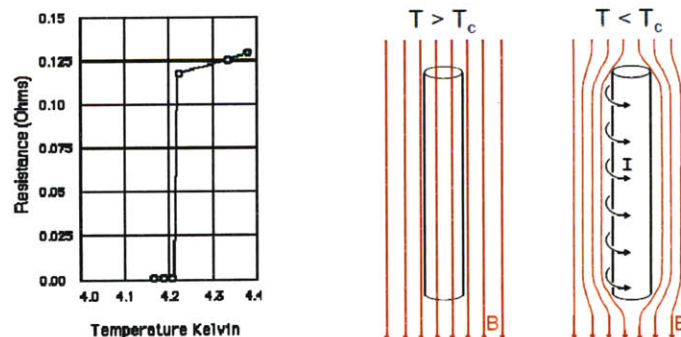
Figure 9. The onset of superconductivity (left) and the Meissner effect (right).[11] A superconductor is characterized by a sudden drop in material resistivity to zero at a critical temperature T_c (left) and by expulsion of magnetic field from the material (right).

Many common materials are superconducting at sufficiently low temperatures. The first superconductor discovered was mercury. Other common materials which exhibit superconductivity include aluminum and lead. Indeed, nearly half of the elements are known to superconduct at sufficiently low temperatures, along with a huge variety of compounds. In most of these materials, superconductivity is well-understood, and essentially explained by conventional BCS theory.

Since superconductors can maintain current flow without requiring a power input and without heat loss, they are ideal for carrying very high currents and therefore creating very strong magnetic fields. The MRI machines used for brain imaging, found in most hospitals, use superconducting wire. NMR, which is an essential tool in chemical characterization, typically requires superconducting magnets as well. These two applications make up a multi-billion dollar market. Also, very high-field magnets used for scientific applications are almost exclusively made of superconducting materials. Typically, these magnets use conventional superconductors. Running these magnets, however, is therefore expensive, due to the helium use required, and high-T_c superconductors are beginning to replace conventional ones in some applications.

There are numerous other applications in which high-T_c superconductors are beginning to make inroads, such as power transmission and storage, wind turbines, maglev trains, and large electric motors such as those in ships. The very high magnetic fields from superconducting magnets, along with their perfect diamagnetism, makes levitation possible, which has amusing applications such as the levitating frog of Figure 10.

Figure 10. A frog levitated by a superconducting magnet.
Photo, with a link to associated video, can be found at the Wikipedia article on magnetic levitation. The frog is unharmed by this experience.

There are several properties that a superconducting material must have in order to find wide application. It should have a high critical temperature, preferably well above 77 K, the boiling point of liquid nitrogen, so that it can be inexpensively and easily cooled. It should be able to tolerate high magnetic fields and high current flow. Finally, it

should be easily and cheaply produced and shaped into wire. In materials which currently exist, these goals cannot all simultaneously be achieved.

Conventional superconductors do not fulfill the first requirement—the most commonly used superconductors have T_c around or under 10K. Some "high temperature superconductors (HTSCs) meet this requirement, but, unfortunately, are not easily turned into wire: they tend to be brittle ceramics. Special, expensive wire production techniques are required, and the resulting wire is not as robust or flexible as traditional copper or aluminum wire. These mechanical issues are the primary obstacle to large-scale adoption of HTSC wire, though much progress has been made in recent years. The original work of this thesis was done on HTSC materials.

1.21 Conventional superconductivity II *

In most materials, electrical resistance occurs when charge carriers, in moving through the material, encounter imperfections in the crystal, such as impurities, missing atoms, distortions in the lattice, or lattice vibrations. In a conventional superconductor below T_c, charge carriers condense into bosonic pairs, known as Cooper pairs, and form a Bose-Einstein condensate which does not easily interact with imperfections in the lattice. Cooper pairs therefore are not scattered and can transport charge without resistance, the hallmark of superconductivity.

The origin and behavior of the pairs is explained by BCS theory.[10] Briefly, Cooper demonstrated that, at sufficiently low temperatures, any attractive potential coupling electrons will lead to pair formation.[8] In most superconductors, this attractive potential arises through coupling to the phonons of the crystal lattice. An electron moving through the lattice attracts positive charges toward itself: this lattice deformation causes another opposite-spin electron to be attracted to the region of the first electron. This pair of electrons with binding energy Δ can only be scattered by events contributing energy greater than Δ to the pair. At sufficiently low temperatures such events will not occur.

By pairing, charge carriers near the Fermi surface lower their energy. For a pairing energy of Δ, pairing leads to depletion of the DOS for states within Δ of the Fermi energy, and enhancement of the DOS Δ away. The depleted area is called the superconducting gap, and the peaks at Δ are called coherence peaks. The density of states is given by:

$$N_s(E) \sim \frac{E}{\sqrt{E^2 - \Delta^2}}$$

Figure 11 shows the DOS for a typical conventional superconductor below T_c.[12]
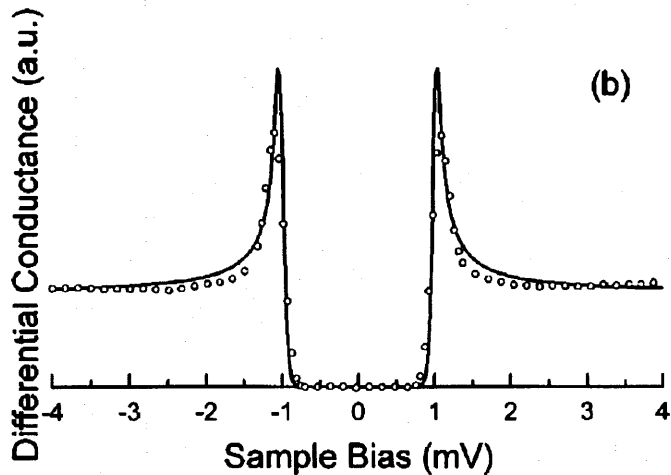
Figure 11. Superconducting gap of Nb at 335 mK.[12]
This spectrum was acquired using a superconducting Nb tip against a Au surface. Symmetry indicates that this is equivalent to using a metallic tip against a superconducting surface.

This gap is most clearly defined at T = 0. As one warms from 0 toward T_c, Δ falls. This effect causes the gap to narrow. Warming also causes thermal broadening, which reduces the resolution with which the DOS can be observed; this often leads to an apparent broadening of the spectra. The combination of these two effects is shown in Figure 12.[12]
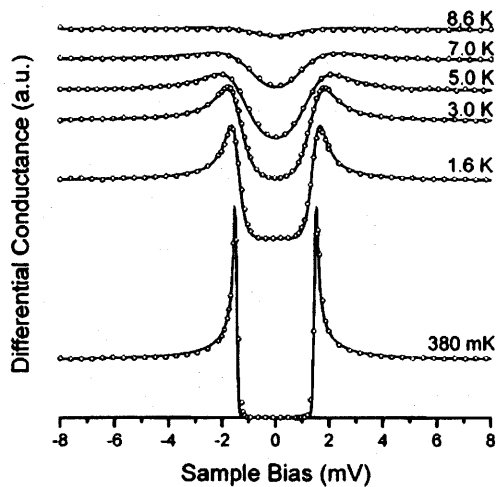
Figure 12. Density of states of Nb at various temperatures.
Spectra are vertically offset for clarity.

BCS theory correctly predicts many features of superconductivity, including the shape and temperature dependence of the gap in the density of states, and the Meissner effect. Until 1986, it was widely believed that superconductivity could not exist in any system above ~28K.[13]

18

1.30 Cuprates and cuprate superconductivity

In most materials, the critical temperature T_c for superconductivity is below 10K. This is too cold to be reached cheaply: typical cooling to this temperature requires the use of liquid helium, an expensive and difficult material to work with.

In 1986, Bednorz and Muller discovered superconductivity at 35K in a new class of layered materials, for which they won the 1987 Nobel Prize in Physics.[14] Soon, crystals similar to theirs showed superconductivity with T_c as high as 92K. This discovery of high-temperature superconductivity (HTSC) was of great scientific and technological importance: scientifically, theories of superconductivity had been thought to imply that superconductivity above 28K was impossible,[13] and revisions were needed to take into account these new materials, perhaps involving fundamentally new physics. Technologically, the high T_c of these new materials made them, in principle, usable in a much wider variety of applications than conventional superconductors. The highest T_c known is 138K as of this writing[15]. While still very cold by conventional standards, this temperature is higher than that of liquid nitrogen (77K), which is a relatively cheap and easily stored coolant. Maintaining temperatures appropriate for superconductivity in these materials is therefore much easier than in conventional superconductors.

The known high-T_c materials are all layered compounds. These crystals consist of sheets, a single atom thick, stacked on top of each other. Most high-T_c superconductors contain layers consisting of copper and oxygen atoms, and it is on these layers that superconductivity is thought to occur. Thus, high-T_c superconductivity is generally modeled as an essentially two-dimensional phenomenon, and most theories of superconductivity focus primarily on these copper-oxygen planes. The work in this thesis is primarily on these so-called "cuprate" superconductors and on related compounds.

The behavior of cuprates depends sensitively on their composition. One commonly-studied high-T_c superconductor is $Bi_2Sr_2CaCu_2O_{8+x}$ (Bi-2212). One unit cell is shown in Figure 13. Note the layered nature of these compounds, which is essential to STM studies. Atomically flat surfaces can easily be obtained by cleaving the system between these layers.
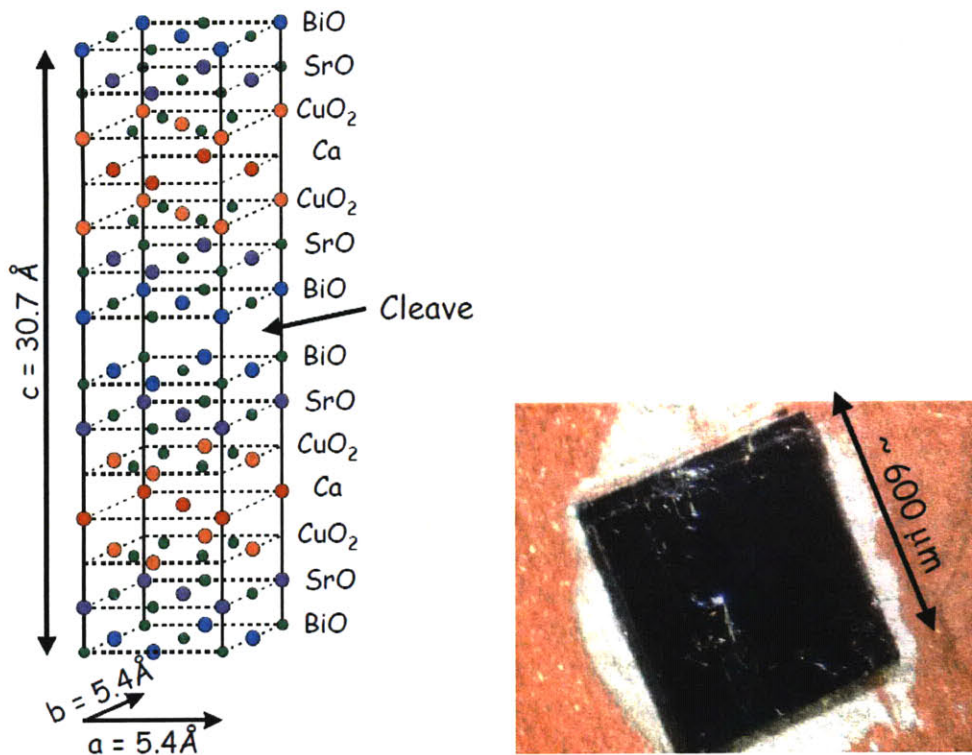
Figure 13. The cuprate superconductor Bi-2212.
One unit cell is shown on the left. Note the layered nature of these compounds. Bi-2212 easily
cleaves between the widely separated bismuth oxide planes, often leaving atomically flat
surfaces behind. On right, a photograph of a single crystal of Bi-2212 mounted on a copper
sample holder.[11]

The x in the chemical formula denotes the presence of extra dopant atoms of oxygen, not shown in the above crystal structure. These atoms add non-stoichiometrically in random positions in the bismuth oxide (BiO) plane, and have both local and global effects. Locally, they affect the density of states[16] and likely the band structure and Fermi surface, as discussed in chapter 3, and thereby contribute to nanoscale inhomogeneity[17,18]. Globally, the number of oxygen dopants alters the superconducting properties of the sample, as illustrated in the generic cuprate phase diagram of Figure 14. The "doping," proportional to the number of oxygen dopants per unit cell x, is along the horizontal axis, and temperature is on the vertical axis.
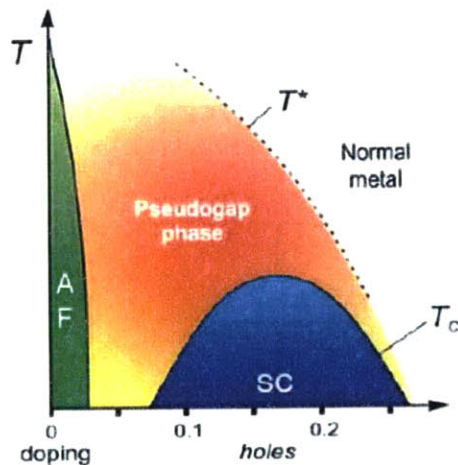
Figure 14. The generic cuprate phase diagram.
Increasing oxygen doping is to the right, and increasing temperature is upward.
Unfortunately, quantitatively correct phase diagrams are not yet known, due in part to the
difficulty of measuring doping.

At low dopings, the system is in an antiferromagnetic insulator state, in which charge carriers are fixed on individual Cu sites and cannot move. In crystals with higher dopings, this insulator breaks down, forming a conducting "pseudogap" state. Superconductivity sets in at around x~0.08, becoming more robust (higher T_c) until x~0.16, then weakening again until vanishing in crystals with x~0.24.

1.31 Band structure in the cuprates *

The cuprate Fermi surface plays an important part in the discoveries described in this thesis. Here I describe the meaning of band structure, and describe the shape and properties of the Fermi surface in cuprates.

Solids can be thought of as gigantic molecules with order 10^{23} electrons. Due to the exclusion principle, no two of these electrons can occupy the same state. In general, we classify the states available for electrons to occupy by the momentum wavevector $\vec{k}$ of the electron in them, and their energy E. Note that an electron classified in this way is primarily wavelike. $\vec{k}$ and E give no information about the spatial location of the electron.

We form the Brillouin zone (BZ) from the set of all $\vec{k}$ available to electrons in the crystal. It turns out that for every wavevector, there are multiple discrete allowed energies $E_{i,kx,ky,kz,s}$, where s denotes the spin degree of freedom. The E_i vary with $\vec{k}$ and therefore form surfaces in k-space (often called "momemtum space" or "reciprocal space"). These surfaces are called "bands" or "energy bands," and we call the shape of these energy surfaces in momentum space the "band structure."

Electrons will fill the lowest energy states available consistent with the exclusion principle and global charge neutrality. We define the Fermi energy E_F as the energy of the highest occupied orbitals, and typically define this to be the zero of our energy scale. The set of all electrons with $E_{i,kx,ky,kz,s}$ equal to E_F is the Fermi surface. It is the electrons

21

on and near the Fermi surface that are the most easily excited, and therefore they determine many of the properties of the crystal.

Most cuprates are approximately two-dimensional, implying the k_z momenta are much more widely spaced than the k_x or k_y. Generally, we ignore the k_z degree of freedom and plot the band structure as a contour map in k_x and k_y, such as in Figure 15.
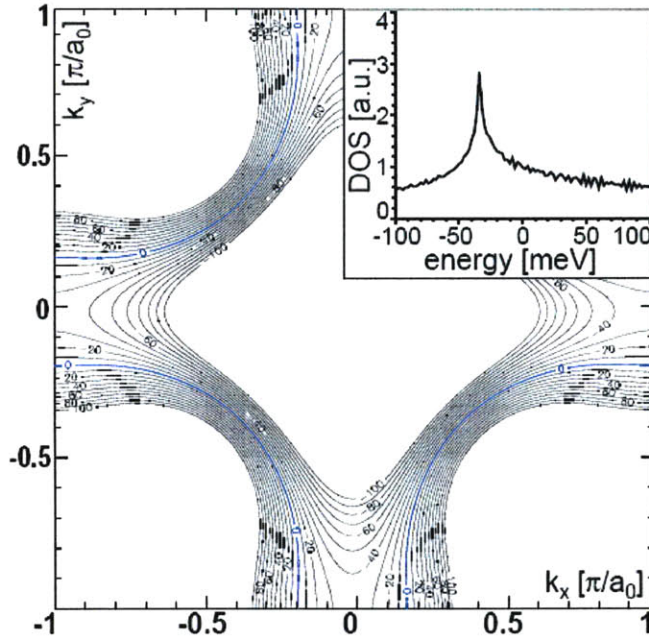
Figure 15. Band structure of Bi2212 in the normal state.[11]
Numbers on contours are energy relative to the Fermi surface. Inset is the density of states integrated over the constant energy contours throughout the Brillouin zone. Zero energy is defined to be the Fermi surface.

The horizontal and vertical directions are called antinodal, and the diagonal directions are nodal. The k_z dependence of this plot is often ignored.

To a first approximation, changes in doping simply shift the Fermi surface, by adding or subtracting holes. Underdoping shifts the Fermi surface onto contours nearer the corners of the above diagram, as illustrated in the schematic diagram of Figure 16, while overdoping shifts the Fermi surface onto contours nearer the center.

22
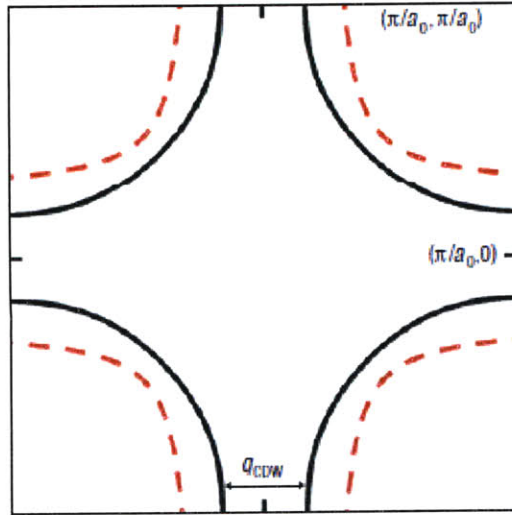
Figure 16. Schematic doping dependence of the cuprate Fermi surfaces.
Black line is a calculated Fermi surface of optimally doped Bi-2201 based on ARPES data.
Underdoping moves the Fermi surfaces towards the corners, illustrated schematically by the
red dashed lines.

1.32 The cuprate phase diagram

In this section, I will discuss the cuprate phase diagram in more detail. In general this section will not be accessible to lay readers.

1.32a Parent compound **

A cuprate with no doping is referred to as the parent compound of the doped material. Conventional solid-state band theory would predict that undoped cuprates would be conductors, as they do not have completely filled valence bands. However, undoped cuprates are in fact insulating, due to the strong interactions between charge carriers, and are part of a class of materials known as Mott insulators.

In the undoped antiferromagnetic (AF) state, one electron occupies each copper atom in the copper oxide plane, and has a spin opposite that of all its neighbors. Each electron cannot leave its lattice site because of strong repulsion from neighboring electrons, so conduction cannot occur.[19]
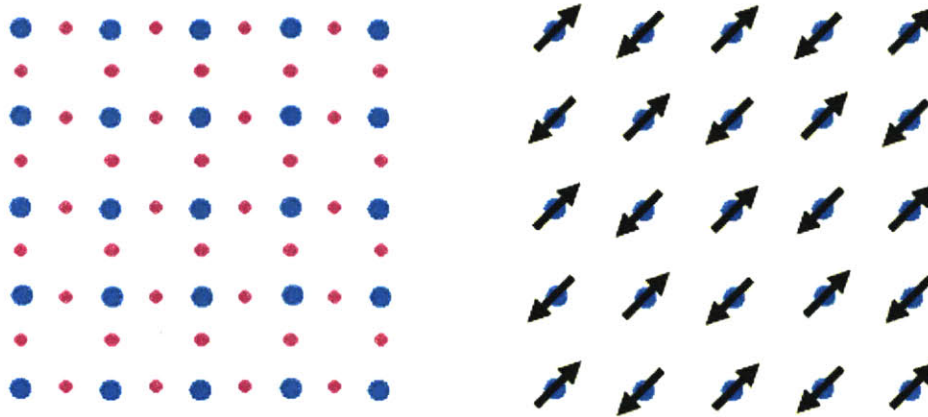
Figure 17. The copper oxide plane (left) and copper atoms with spins (right).[4]
On left, blue circles represent Cu atoms and pink circles O atoms, showing the structure of the copper oxide plane. On right, the antiferromagnetic ordering of electrons in the undoped "parent" compound is illustrated. Electrons cannot "hop" from one copper atom to the next because of on-site repulsion. The compound is thus an insulator.

Oxygen doping changes this picture. Oxygen, being highly electronegative, will bind electrons to itself, removing them from the lattice. This process creates "holes," copper sites in the lattice that are unoccupied by electrons. The presence of these holes allows electrons to move, hopping between occupied and unoccupied states, and thus allows conduction to occur, and the breakdown of the AF insulator state. In cuprates, superconductivity somehow arises from this "doped" state.
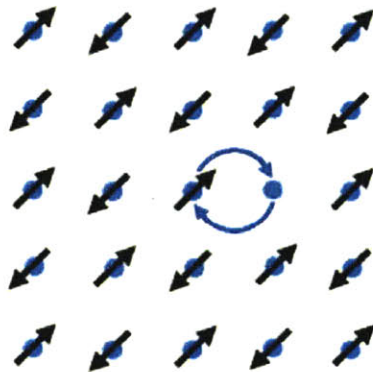
Figure 18. Effects of hole doping.
Hole doping opens spots into which electrons can move. Doping thus allows conduction to occur.

1.32b High-T$_c$ superconductivity **

Outside the AF insulator part of the phase diagram, we find the pseudogap and superconducting phases, neither of which is fully understood. In this section, I will not give a full account of high-T$_c$ superconductivity; instead, I will focus primarily on those phenomena most relevant to understanding the remainder of this thesis. The pseudogap will be discussed in the following section.

High temperature superconductors have much in common with conventional superconductors. Both display the Meissner effect, and are typically extreme type II superconductors. Cooper pairs still form in high-T_c superconductors,[20] though the mechanism of Cooper pair formation in the cuprates is still debated. The density of states is still gapped. However, the shape of this gap differs: this is because high-T_c superconductors are d-wave superconductors, in contrast to the primarily s-wave conventional superconductors. Explaining this statement and its implications will take up the bulk of this section.
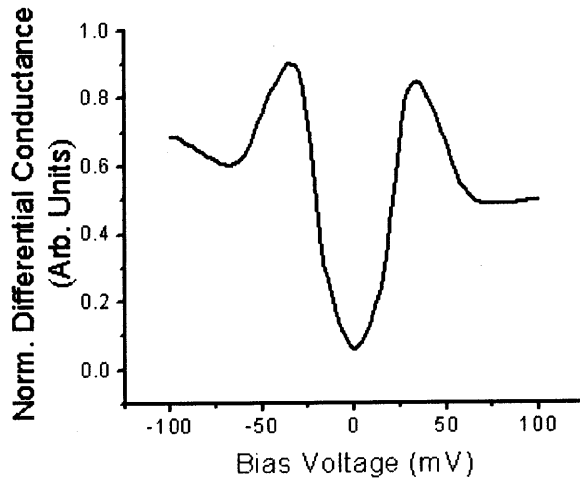
Figure 19. Spectrum from superconducting Bi-2212.

Figure 19 shows a superconducting spectrum from Bi-2212. The obvious difference from the spectrum of a conventional superconductor is that the DOS is non-zero everywhere except at the Fermi energy. This is a characteristic property of d-wave superconductors. To understand this, we must look into reciprocal space.

An STM has no inherent k-space resolution; it measures electrons in all directions in momentum space. Spectra measured by STM are therefore is an average over k-space.

Conventional superconductors are s-wave superconductors; this means they have no symmetry beyond that of the crystal lattice. The opening of the gap eliminates the Fermi surface contour and pushes constant-energy contours away from the Fermi surface. Figure 20 illustrates this.
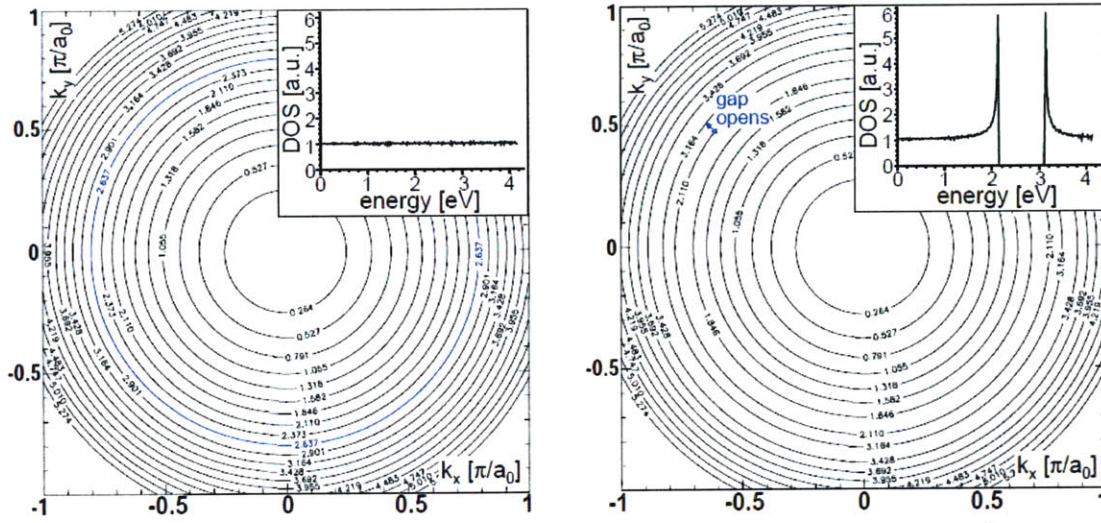
Figure 20. Band structure and gapping of hypothetical s-wave superconductor.[11]
Blue line represents the Fermi surface. In the normal state (left), this hypothetical material has a continuous, circular Fermi surface and a density of states which is constant in energy (inset). On right, a superconducting gap eliminates the Fermi surface and opens up a gap between the equipotential lines, yielding a gap in the density of states (inset).

In a d-wave superconductor, the gap has $d_{x^2-y^2}$ symmetry; the gap is stronger for particles travelling in some directions in k space than in others, implying that the gap in the DOS is a function of angle. The density of states is then given by an integral of an angle-dependent gap over all directions:

$$N_s(E) \sim \int_0^{2\pi} \frac{E}{\sqrt{E^2 - (\Delta_0 \cos(2\theta))^2}}$$

The difference in $\Delta(k)$ is illustrated in Figure 21.
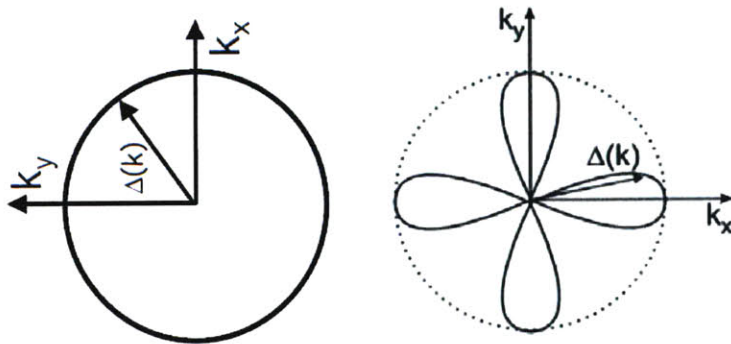
Figure 21. Gap magnitude versus angle in superconductors.
In s-wave superconductors (left), the gap magnitude is constant in all directions in k-space. In d-wave superconductors (right), the gap magnitude varies strongly with angle, with its magnitude going through maxima at 0, $\pi/2$, π... and minima at $\pi/4$, $3\pi/4$,....[11]

26

Note that the gap magnitude in the d-wave case falls all the way to zero in the [1,1] ("nodal") direction; this implies that in this direction the Fermi surface is not gapped at all. At 45 degrees from this, in the "anti-nodal" direction, the gap has its maximum value. In general, there are a wide variety of gap sizes, depending on the direction of the electron's momentum. The STM, having no k-space resolution, averages over all of these gaps; this explains the distinctive V-shape of the d-wave spectrum near the Fermi energy. (Our knowledge of the band structure of the cuprates comes primarily from other experimental techniques, particularly ARPES.)

Recall the Fermi surface of the cuprates, resembling quarter-circles centered on each corner of the Brillouin zone (Figure 16). The effect of a d-wave gap on the Fermi surface and band structure is shown here.
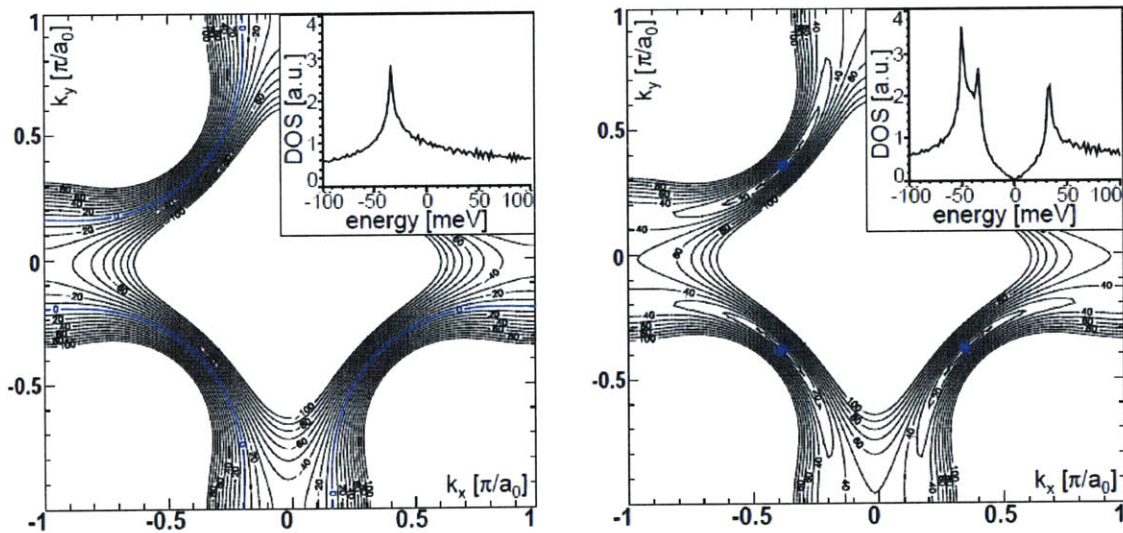
Figure 22. Effect of the superconducting gap in k-space.[11]
An ungapped band structure (left) has a Fermi surface (blue lines) surrounding hole pockets in the corners. Adding d-wave superconductivity (right) eliminates the continuous Fermi surface. The only electrons at the Fermi energy are those at 45 degrees (blue dots). The rest of the Fermi surface is gapped away.

Using ARPES, one can measure the dependence of Δ on angle. Such measurements, such as those of Figure 23, confirm that the superconducting gap is roughly d-wave in the cuprates.[21]
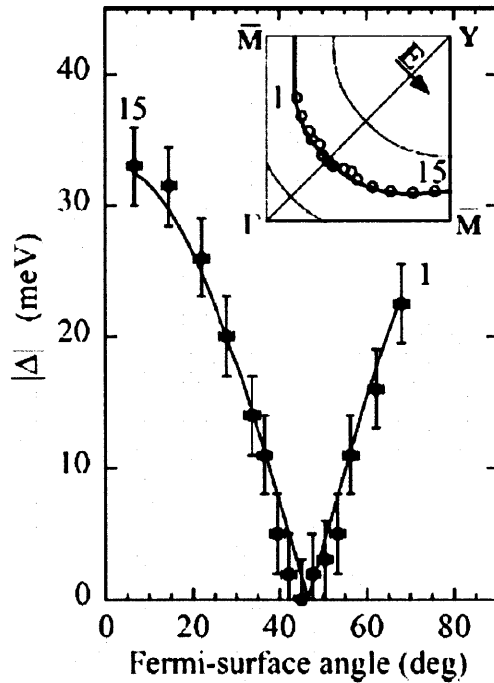
Figure 23. Gap in superconducting Bi-2212 as a function of k-space angle.[22]
The gap magnitude in Bi-2212 is fitted by the d-wave symmetric function cos(kx)-cos(ky) (solid line). The gap falls to zero at 45 degrees and approaches a maximum at 0 and 90 degrees. In contrast, the gap of an s-wave superconductor is independent of angle.

1.32c Pseudogap **

Recall that the density of states of a conventional superconductor is gapped. The gap size Δ falls as a function of temperature, reaching zero at T_c. In the cuprates, on the other hand, a d-wave gap exists in the superconducting region. However, this gap does not disappear at T_c: instead, it gradually fades in strength, going away at some higher temperature called T^*, as illustrated in by STM in Figure 24.[23] The region of the phase diagram in which a gap exists, but superconductivity does not, is the pseudogap region, and we refer to the gap that exists between T_c and T^* as the pseudogap.
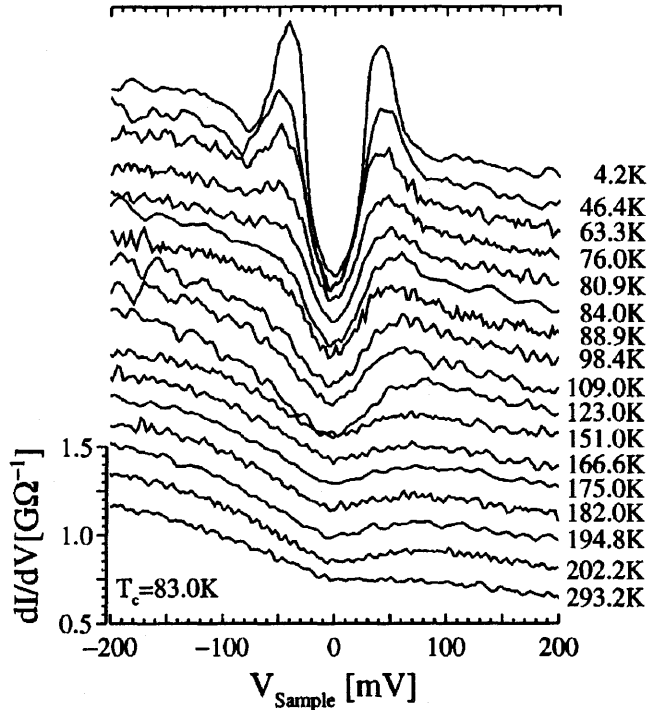
**Figure 24. Temperature dependence of Bi-2212 spectra (UD83K).
Spectra are vertically offset for clarity.**[23]

In k-space, it is believed that the nodal region of the sample consists of ungapped arcs, called "Fermi arcs," above T_c, while the anti-nodal region remains gapped until T^*.[24] In the intermediate temperature range, the Fermi arcs grow with increasing temperature until a complete Fermi surface forms by T^*.[25]

The nature of the pseudogap is not yet clear, in spite of extensive research. There are two main classes of theories: one in which the pseudogap is seen as a precursor to superconductivity, and another in which the pseudogap is a sign of a separate order, unrelated to superconductivity.

The pseudogap states have been associated with a so-called "checkerboard" electronic ordering, which has been observed in the cuprates both above and below T_c in various systems.[26,27,28] A system will order when it can lower its energy by doing so; this means that electronic ordering may create an gap in the electronic density of states. This checkerboard, then, may be an important clue as to the nature of the pseudogap state. Chapter 2 of this thesis will discuss this in much more detail.

29

2.0 Checkerboard order in the cuprates *

     This is the first section of this thesis that describes original research done as a part of my PhD. Here, I attempt to give a brief overview of one of our papers, in a way that is understandable to non-specialists. The paper is Nature Physics 4, 696-699; "Charge-density-wave origin of cuprate checkerboard visualized by scanning tunneling microscopy.[1]" Sections 2.1 onward are technical and are almost identical to that paper. These sections will not be understandable except to those in the field.

     As discussed in section 1.32c, spectral surveys of the pseudogap state of the cuprates have often found that a spatially modulated "checkerboard" electronic order superimposed on the density of states. The first observation of such a checkerboard was made by the Yazdani group in 2004[26], in which it was observed above T_c in Bi-2212.
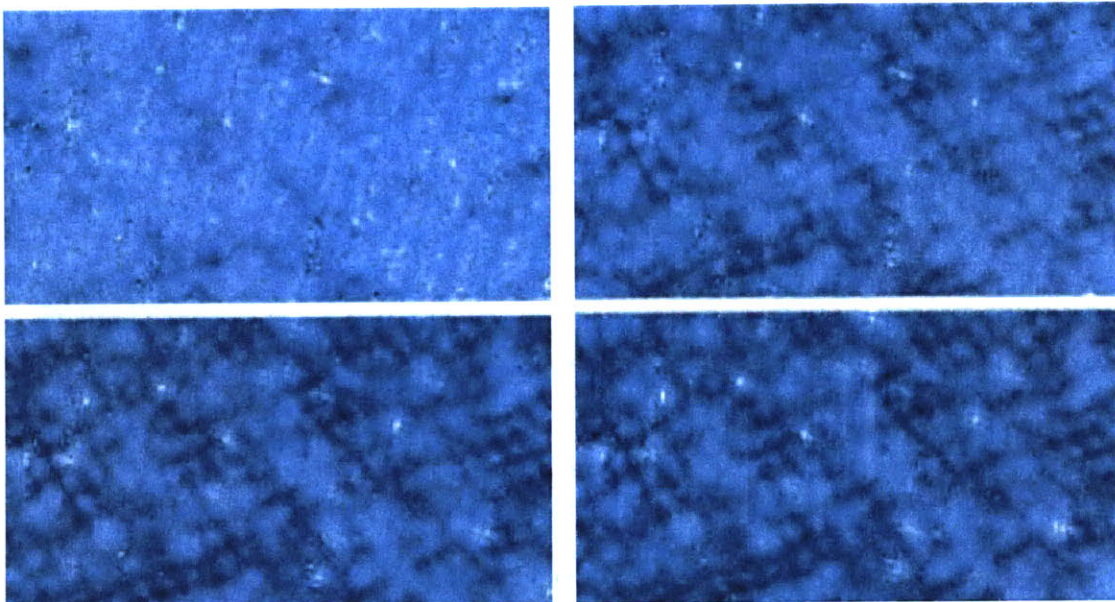
Figure 25. Checkerboard ordering above T_c in Bi-2212.
Checkerboard ordering in slightly underdoped Bi-2212 (T_c=80K) at T=100K is revealed by conductance maps at various energies. Shown are maps taken at 41 mV (top left), 24 mV (top right), 12 mV (bottom left), and 6 mV (bottom right), and published by the Yazdani group.[26]

     Another influential early observation was by the Davis group, of a commensurate checkerboard in Na-CCOC.[28]
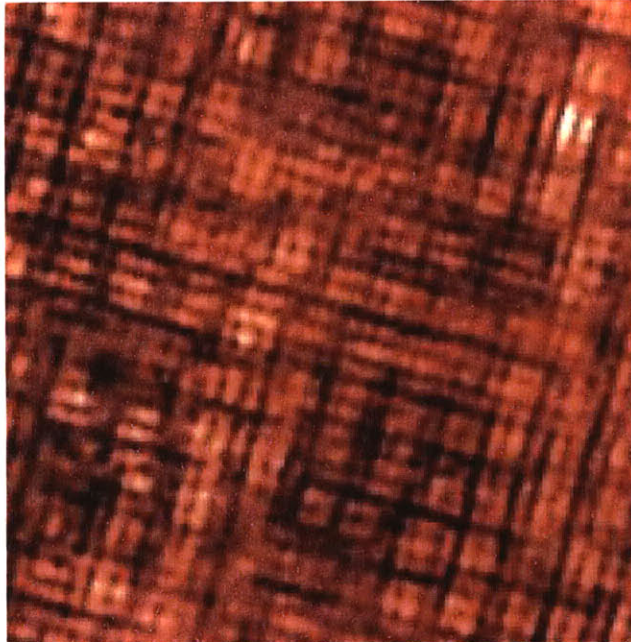
Figure 26. Checkerboard ordering in Na-CCOC.
Checkerboard ordering in Na-CCOC. Shown here is the 8 mV layer, taken at 4K. The period of the checkerboard is exactly $4a_0$.[28]

In previous studies of this checkerboard, it has been observed to have a period of roughly four times the lattice constant a_0. This ordering is non-dispersive; that is, the wavelength does not change as a function of the energy under observation. This behavior is therefore different than the quasiparticle interference patterns (QPI) which will be discussed in chapter 3. The checkerboard is not perfectly regular; it in fact has a rather short correlation length in all compounds studied.

This checkerboard must exist because the sample can minimize its energy through ordering. Thus, the checkerboard may contribute to or cause other aspects of the pseudogap phase. For example, the pseudogap phase is characterized in part by a gap in the density of states, and many electronic spatial ordering phenomena might simultaneously cause checkerboard-like ordering and a gap in the density of states.

We have carried out a systematic study of the checkerboard as a function of temperature and of doping, through a series of spectral surveys on different crystals. Our findings, in short, are that in Bi-2201, the checkerboard exists throughout a large section of the phase diagram, that the wavelength of the checkerboard increases with increasing oxygen doping, and that it is independent of temperature.

These findings can be checked against various theories of the checkerboard. We find that most theories are inconsistent with at least one of these results, and can be ruled out by our observations. One theory that *is* consistent with our findings is that the checkerboard is due to a so-called charge density wave (CDW). A CDW is also typically associated with a gap in the density of states, which could very directly connect the pseudogap to CDW ordering. A significant amount of the behavior of the pseudogap phase would be explained by this.

Of course, we have not proved that the checkerboard is associated with a CDW— such proof can only come from the accumulation of numerous results from different

31

experimental techniques. Also, it is likely that other theories will arise that are consistent with our results. However, we have provided a strong constraint that theories of the checkerboard must meet.

2.1 Charge-density wave origin of cuprate checkerboard ***

As noted earlier, this section is almost identical to our paper in Nature Physics[1] and is reproduced here with permission. The main changes are to formatting.

A great deal of current interest is focused on the 'checkerboard'-like electronic lattices first discovered in cuprates by scanning tunnelling microscopy (STM) in vortex cores in optimally doped $Bi_2Sr_2CaCu2O_{8+\delta}$ (Bi-2212) (ref. 29). This ordering was found to have a roughly 4 unit-cell ($4a_0$) wavelength orientated along the Cu–O bond direction. Subsequent STM investigations of the cuprates have revealed other checkerboard structures in the absence of a magnetic field. For example, in the superconducting state of Bi-2212, the first report of a checkerboard saw a roughly $4a_0$ wavelength throughout the sample[30], whereas a later study found the ordering (wavelength $4.5a_0$) limited to regions with large-gap ('zero-temperature pseudogap') tunnelling spectra[27]. A checkerboard was also found in slightly underdoped Bi-2212 above the superconducting transition temperature Tc with wavelength $4.7a_0\pm0.2a_0$ (ref. 26). In $Ca_{2-x}Na_xCuO_2Cl_2$ (Na-CCOC), a commensurate electronic crystal phase with period $4a_0$ was found at low temperatures in both superconducting and non-superconducting samples[28].

Although it is not yet clear whether these checkerboards all represent the same electronic entities, many models have been proposed to explain the mechanisms of these novel electronic phases and their implications for the pseudogap and high-Tc superconductivity[31-38]. Initially, it was suggested[29,32] that the $4a_0$ pattern in Bi-2212 vortex cores is the charge-density modulation accompanying the $8a_0$ spin-density wave (SDW) created by an external magnetic field. Other explanations of checkerboards include exotic orderings such as fluctuating one-dimensional stripes[33], modulations of electron hopping amplitude[34], Cooper pair Wigner crystal[35] or density wave[36] and orbital-current-induced d-density wave[38]. Recently, angle-resolved photoemission spectroscopy (ARPES) on Na-CCOC found parallel Fermi surface segments with a nesting vector around $2\pi/4a_0$ in the antinodal region, suggesting charge-density-wave (CDW) formation as the origin of the checkerboard[39]. Unfortunately, existing data are inadequate to discriminate between the different models, mainly because the experiments were carried out on small, isolated regions of the complex cuprate phase diagram.

Here, we report on systematic doping- and temperature-dependent STM studies of charge-density modulations in the high-temperature superconductor $Bi_{2-y}Pb_ySr_{2-z}La_zCuO_{6+x}$ (Pb- and La-substituted Bi-2201) (ref. 40). We find that a static (non-fluctuating), non-dispersive (energy-independent), checkerboard-like electronic lattice exists over a wide range of doping, and that its wavelength increases with increasing hole density. This unexpected trend strongly supports the physical picture of Fermi-surface-nesting-induced CDW formation and is corroborated by comparison to band-structure calculations and ARPES measurements.

These experiments were conducted on a home-built variable-temperature STM, which enables simultaneous mapping of atomic-scale topography and differential conductance spectroscopy, proportional to the energy-dependent local density of states (LDOS) of the sample. We begin by describing our results on optimally doped Bi-2201 with Tc=35 K. Figure 27a shows a typical atomic-resolution STM topography of a 785-Å region measured at T=6 K. The inset shows the Pb (brighter) and Bi (dimmer) atoms of the exposed BiO plane. The CuO_2 plane lies ~5 Å below. A representative differential conductance spectrum from this area (Figure 27b) has a clear inner gap with peaks near 15 meV, probably associated with the superconducting gap, and a pseudogap with size roughly 75 meV (ref. [41]). A differential conductance map of the region taken at a bias of 10 meV (Figure 1c) shows a checkerboard-like electronic lattice, strikingly similar to those observed in other cuprates[26-28,30]. The checkerboard is observed to beyond 50 meV at both positive and negative sample bias, although the pattern appears most strongly at low, positive bias. It appears in maps taken with feedback setpoint voltages ranging from 10 to 300 mV, with feedback currents from 50 to 800 pA, and in topographic scans at 10 mV bias.
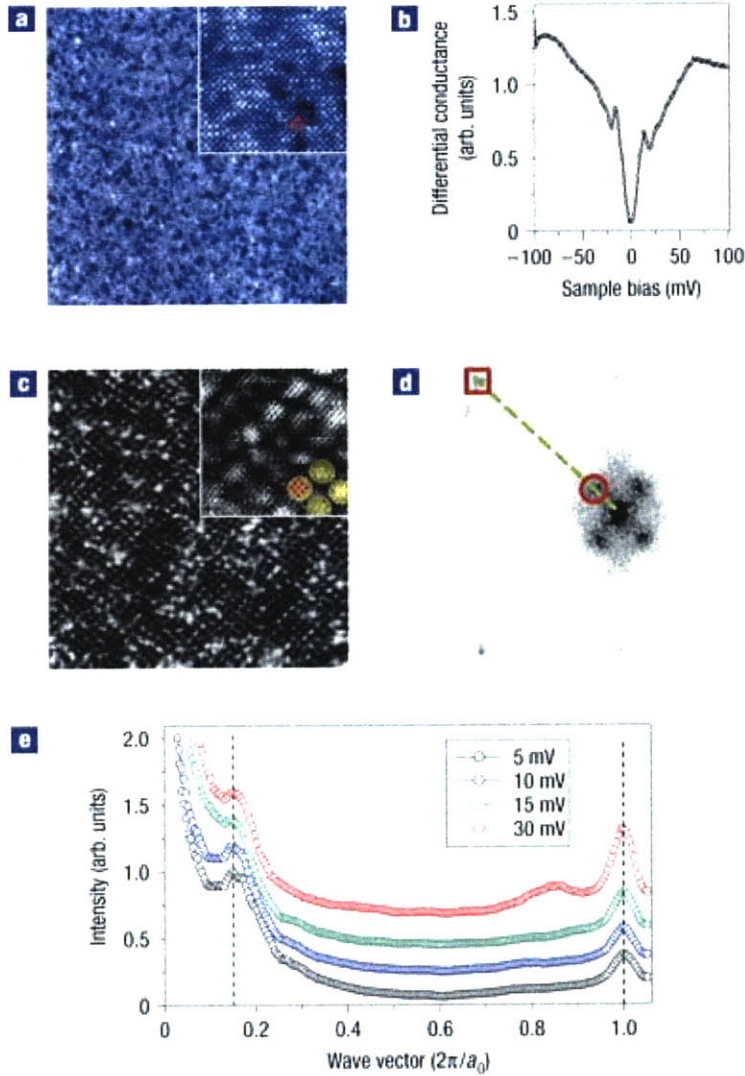
Figure 27. Checkerboard ordering in optimally doped Bi-2201.
a, STM topography of a 785-Å region of optimally doped (T_c=35 K) Bi-2201 measured at T=6 K. The magnified inset (110 Å) (and red dots on 9 atoms) show the clear atomic lattice in this high-resolution data. b, Spatially averaged differential conductance spectra measured in the area shown in a exhibit two distinct gaps: a superconducting gap $\Delta_{SC} \sim 15$ meV and pseudogap $\Delta_{PG} \sim 75$ meV. c, Conductance maps, here taken with bias voltage 10 meV on the same region as a, show a checkerboard structure in the LDOS with a wavelength much larger than the atomic lattice. The inset is magnified as in a, with the same 9 atoms highlighted in red. Four checkerboard maxima are also highlighted (yellow) for clarity. d, Fourier transform of the map shown in c. The checkerboard wave vectors (circled) appear as four spots along the same direction as the atomic lattice (outlined with a square). The dashed line shows the locations of the line cuts in e. e, Line cuts extracted from Fourier-transform LDOS maps with different bias voltages. The left vertical line marks the position of the checkerboard wave vector, $2\pi/6.2a_0$ for all energies, and the right vertical line indicates the atomic lattice wave vector $2\pi/a_0$. All data in this letter was acquired with feedback setpoint parameters I_S=400 pA and V_S=-100 mV or V_S=-200 mV.

34

The wavelength of this checkerboard is determined from the Fourier transform of the image, as shown in Figure 27d, where the checkerboard appears as four peaks (one is circled). Its wave vector corresponds to a wavelength $d \sim 6.2a_0 \pm 0.2a_0$, much larger than that of any such structure previously reported. Figure 1e shows a line cut along the atomic lattice $(\pi, 0)$ direction of the Fourier-transform LDOS maps taken at different bias voltages. The consistent position of the checkerboard wave vector observed at different energies, marked by the left dashed line, indicates that the checkerboard is a non-dispersive, static ordering.

We find similar checkerboard structures in underdoped Bi-2201 samples with Tc=32 K (Figure 28b) and Tc=25 K (Figure 28c). Surprisingly, Fourier transforms reveal that checkerboard periodicities in these underdoped samples are reduced to $5.1a_0 \pm 0.2a_0$ and $4.5a_0 \pm 0.2a_0$ respectively, significantly shorter than in the optimally doped sample. This can be seen directly from the denser packing of the underdoped checkerboard (Figure 28b,c) compared with that in the optimally doped one (Figure 28a). Figure 28d summarizes this doping dependence in line cuts of the Fourier transforms along the atomic lattice $(\pi, 0)$ direction. The increase of the checkerboard wave vector with decreasing hole density is pronounced.
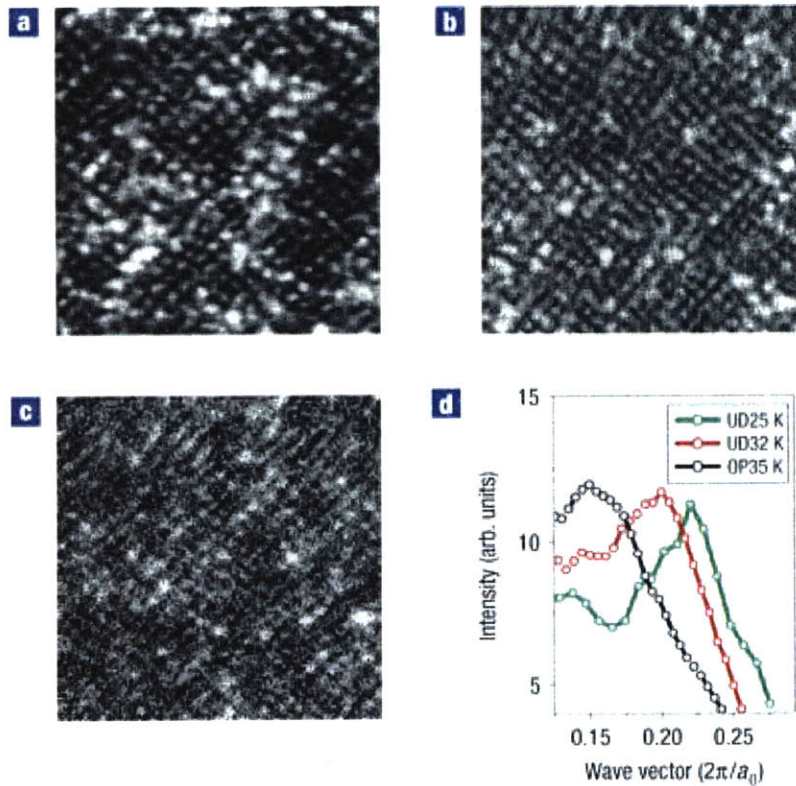
Figure 28. Doping dependence of the cuprate checkerboard.
a–c, 400 Å conductance maps of optimally doped, Tc=35 K (a), underdoped, Tc=32 K (b), and underdoped, Tc=25 K (c), Bi-2201. All maps were taken with 10 mV sample bias at T=6 K. The checkerboard structures shown in b,c have denser packing than in a, indicating a shorter wavelength in underdoped samples. d, Line cuts along the atomic lattice direction of the Fourier-transform LDOS maps of the three samples. The cuts peak at the checkerboard wave vectors, corresponding to wavelengths of $6.2a_0$, $5.1a_0$ and $4.5a_0$, respectively.

In contrast to doping, temperature has no measurable effect on the checkerboard wave vector. The LDOS map of the underdoped Tc=32 K sample measured at 35 K (Figure 29a) is qualitatively the same as that measured at 6 K (Figure 28a). Figure 29b shows line cuts of the Fourier transforms of maps measured at a wide range of temperatures, demonstrating that the peak location is unaffected by temperature and in particular T_c.
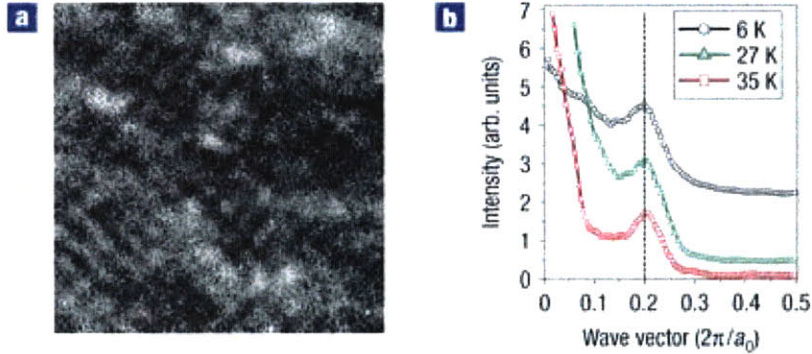
Figure 29. Temperature dependence of the cuprate checkerboard.
a, 300 Å, 10 mV conductance map of the underdoped Tc=32 K sample measured at T=35 K, slightly above Tc. The checkerboard is qualitatively unchanged from low temperatures (Figure 28b). b, Line cuts along the atomic lattice direction of Fourier-transform LDOS maps at this and lower temperatures indicate that the checkerboard wave vector is temperature independent (vertical line).

These results reveal important new features of the checkerboard. First, the non-dispersive charge-density modulation found previously in Bi-2212 (refs 26,27,30) and Na-CCOC (ref. 28) also exists in Bi-2201, suggesting that it is a robust feature that prevails in the cuprate phase diagram, in both optimally doped and underdoped phases, and at temperatures both below and above T_c. More importantly, the doping dependence of the checkerboard periodicity puts stringent constraints on relevant theoretical models, as discussed below.

We first emphasize that the checkerboard structures reported here and previously[26-28,30] are distinct from the spatial LDOS modulations induced by quasiparticle interference[42] (QPI). QPI wave vectors depend strongly on energy because they are formed by interference of elastically scattered quasiparticles residing on equal-energy contours of the Fermi surface[43]. In contrast, the checkerboard lattice is non-dispersive. Quantitatively, modeling QPI (ref. 43) using a tight-binding Fermi surface[44] and $\Delta=\Delta_0\cos(2\theta)$ with Δ_0=15 mV suggests that the QPI vector closest to these checkerboard peaks would disperse from about 0.18 ($2\pi/a_0$) to 0.33 ($2\pi/a_0$) over the energy range shown in Figure 27, clearly inconsistent with the non-dispersing vectors we report here. Similarly, QPI from the ends of the Fermi arcs[45], a seemingly reasonable explanation of the checkerboard observed strictly above Tc in Bi-2212 (ref. 26), cannot explain the temperature-independent, non-dispersive pattern reported here. Although we have observed wave vectors associated with QPI Bi-2201, we defer discussion of these interesting features to a future paper.

For non-dispersive checkerboard formation, a number of explanations have been proposed. Most predict a checkerboard wavelength that decreases with doping, opposite to our results. For example, the presence of a $4a_0$ checkerboard in Bi-2212 vortex cores[29] was initially attributed[29,31,32] to the long-sought concomitant charge modulation of the 8a0 SDW found earlier by neutron scattering in the vortex lattice state of $La_{2-x}Sr_xCuO_4$ (ref. 46). In a variety of cuprates, neutron scattering experiments have found incommensurate SDWs, which should create accompanying charge-density modulations with half the wavelength[31,32]. Although this is an appealing picture for the vortex checkerboard, that the measured SDW wavelength decreases with increasing doping[47] means it cannot explain the patterns reported here.

The stripe model[34], which posits that fluctuating stripes can form a checkerboard-like pattern when pinned by impurities, also predicts that wavelengths should decrease with doping, as more holes means more stripes and a smaller average distance between them. Similarly, in theories that attribute checkerboard patterns to real-space organization of Coulomb-repulsed Cooper pairs in the form of Wigner crystals[35] or Cooper pair density waves[36], the distance between neighbouring Cooper pairs would be expected to decrease with doping as the Cooper pairs become less dilute. These predictions are also at odds with our observations.

We propose that the most likely origin for the checkerboard is the formation of an incommensurate CDW (ref. 37). The cuprate Fermi surface flattens out in the antinodal $(0,\pi)$ region and forms parallel ('nested') sections there (Figure 30). Nesting benefits the formation of CDWs, as a modulation at a single wave vector can gap large sections of the Fermi surface and lower electronic energy. With fewer holes in the CuO_2 plane in underdoped samples, the cuprate hole-like Fermi surface shrinks (dashed line), leading to a larger nesting wave vector and hence smaller real-space wavelength, in agreement with the doping dependence we report here.
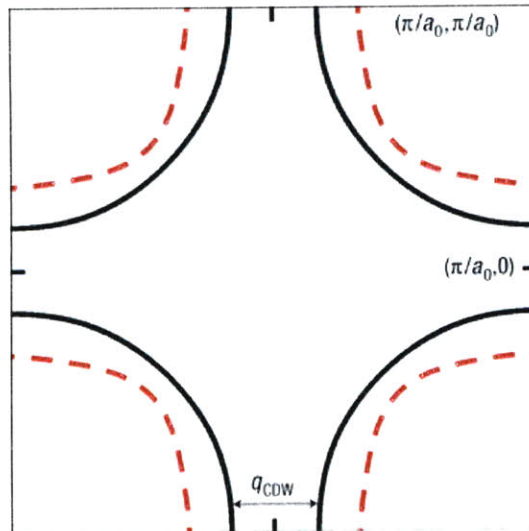
Figure 30. Schematic doping dependence of cuprate Fermi surface.
Tight-binding-calculated Fermi surface (solid black curve) of optimally doped Bi-2201 (ref. [44]) based on ARPES data[48]. The nesting wave vector (black arrow) in the antinodal flat band region has length $2\pi/6.2a_0$. Underdoped Bi-2201 Fermi surfaces (shown schematically as red dashed lines) show a reduced volume and longer nesting wave vector, consistent with a CDW origin of the doping-dependent checkerboard pattern reported here.

The CDW picture can also explain the checkerboards in Bi-2212 and Na-CCOC. ARPES measurements on slightly underdoped Bi-2212 reveal an ~$2\pi/5a_0$ antinodal nesting wave vector[49], in agreement with the STM-measured $4.7a_0$ checkerboard periodicity[26]. In Na-CCOC, the match of the $4a_0$ checkerboard wavelength to their ARPES-measured nesting wave vector around $2\pi/4a_0$ also led researchers to the conclusion of a CDW (ref. 39). The doping dependence sought in that study, but absent in the invariably commensurate $4a_0$ checkerboard, possibly owing to lock-in of an incommensurate CDW by the crystal lattice, is revealed here in Bi-2201, where the checkerboard is incommensurate and strongly doping dependent, clearly favouring a Fermi-surface-nesting-induced CDW picture.

With a CDW as the most likely source of the checkerboard, we next turn our attention to the relationship between this CDW and other physics in the system. In particular, because we observe it both above and below T_c, the question arises as to whether the CDW is the hidden order of the pseudogap phase. Recent discovery of a dichotomy between the nodal and antinodal quasiparticles, revealed by Raman and ARPES experiments[50-52], supports this conjecture. Quasiparticles near the node have a d-wave gap that opens at T_c, and hence are assumed to be responsible for d-wave superconductivity. Quasiparticles near the antinode on the other hand have a large gap that is roughly temperature independent near, and exists well above, T_c. That this gap persists above T_c demonstrates that it is the pseudogap. That this gap exists near the antinodes, where the nested Fermi surface seems responsible for the formation of the CDW we report here, suggests that the pseudogap may be the CDW gap.

Objecting to this claim, some have commented that a CDW gap need not be centred on the Fermi energy and thus at least at some dopings the pseudogap should be asymmetric around it. Close observation of our spectra affirms that the pseudogap is rarely symmetric about the Fermi energy. Figure 27b shows peaks at -88 meV and +66 meV, very asymmetric particularly considering the clear symmetry of the inner (superconducting gap) peaks at ±15 meV. This asymmetry is ubiquitous in large-gap regions (see for example Fig. 1a of ref. 26 and Fig. 2b of ref. 27), where the pseudogap is clearly distinguishable from the symmetric superconducting gap, blunting this objection to the picture of the pseudogap as the CDW gap.

Although a nesting-driven CDW explanation of the checkerboard is generally consistent with our data, there remain unresolved issues that require further experimental and theoretical exploration. ARPES measurements of the Fermi surface nesting vector of Bi-2201 by different groups contain significant disagreements, making quantitative numerical comparisons of the checkerboard wave vector to the nesting wave vector across dopings difficult (although the qualitative doping dependence is certainly in agreement with our results). ARPES also suggests that the antinodal states in the cuprates may be incoherent, and the mechanism by which a CDW would arise from incoherent states is unclear.

Furthermore, if a CDW existed in these samples, it could in principle be observed in scattering experiments, but no such observation has yet been reported. This may in part be due to the weak, glassy nature of these modulations[53]. Although X-ray has successfully detected charge modulations in $La_{2-x}Ba_xCuO_4$, the inplane correlation length there (ξ~500 Å) (ref. 54) is significantly longer than in Bi-2212 (ξ~90 Å) (ref. 26), Na-

38

CCOC ($\xi\sim40$ Å) (ref. 28) and in the Bi-2201 samples discussed here ($\xi\sim35$ Å), perhaps owing to pinning by disorder in these samples. This difference alone would be responsible for a drop in scattering signal of a couple orders of magnitude for some techniques, and may thus explain the lack of corroborating results from scattering experiments.

Thus, despite similarities between CDWs, the checkerboard and features of the pseudogap, much work remains to be done before confirming or refuting this picture. The pseudogap is a rich phase, exhibiting a wide variety of phenomena and, so far, no theory has consistently explained all of the results of the large number of experimental probes of its nature. That the CDW discussed here explains some of them is a beginning.

3.0 Local Fermi surface changes in the cuprates **

Here, I describe a second piece of original research done for this thesis. As in chapter 2, I begin with a brief, hopefully accessible description of the scientific results. The second section contains a technical description of the results, largely based on our paper, "Imaging nanoscale Fermi-surface variations in an inhomogeneous superconductor," first published in Nature Physics.

In chapter 1, I introduced the idea of band structure, which describes the distribution of electrons in momentum space (the Brillouin zone). The Fermi surface divides that volume of the band structure that is occupied by electrons from the unoccupied volume. The cuprates, being essentially 2D compounds, have largely two-dimensional band structure, with a Fermi surface that changes with doping as shown previously in Figure 16.

Since the STM has no direct k-space resolution, much of what we know about cuprate band structure comes from other techniques. However, band structure does affect the real-space density of states, in ways that can be examined by STM. In particular, the shape of the Fermi surface gives rise to standing waves in real-space. STM observes these waves. From the angle and spacing of these waves, the shape of the Fermi surface can be inferred.

There are two types of electronic waves that we can observe. One is based on quasiparticle interference (QPI) and the other is based on the cuprate checkerboard, discussed in the previous section.

Quasiparticle interference patterns come from interference between parts of the Brillouin zone with especially high density of states. In the cuprates below Tc, such points are believed to fall on the Fermi surface. By observing the waves generated by quasiparticle interference as a function of energy, part of the Fermi surface can be reconstructed.
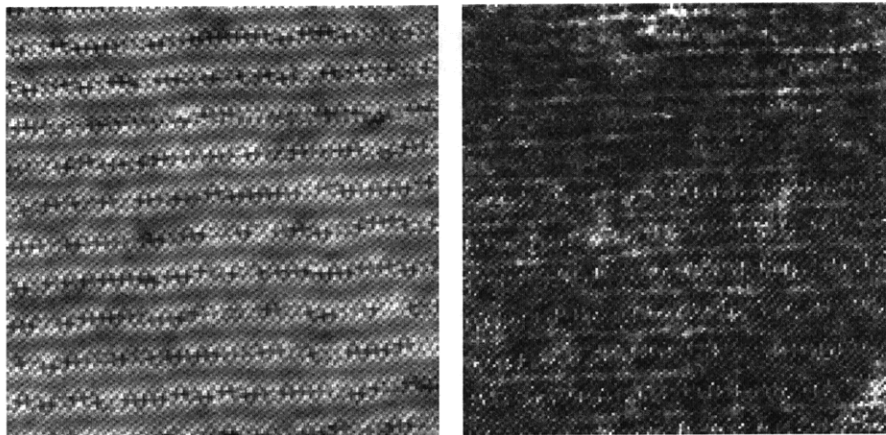
Figure 31. Surface waves from quasiparticle interference in Bi-2212.
240Å topography (left) and simultaneously acquired spectral survey (right), in overdoped Bi-2212 (OD89K). Multiple periodic structures can be seen in the spectral survey.

The other surface wave we use is the checkerboard pattern described in chapter 2. The wavevector of this checkerboard is tied to the separation of the antinodal sections of the Fermi surface (see Figure 28 and Figure 30).

Together these two techniques give a reasonably complete picture of the Fermi surface.

The checkerboard and quasiparticle interference patterns have been extensively studied before. However, previous reports have looked only at the average wavelength of the checkerboard throughout the sample. Similarly, quasiparticle interference patterns have only been analyzed globally. The innovation I present here is to extend these studies to a local scale.

We perform checkerboard analysis on those sections of the sample with small gaps in the DOS, and then on those sections of the sample with large gaps. We find that the result is different for each of these analyses. QPI analysis, too, differs when performed on regions with large and small gaps. Finally, we are able to do this analysis in real-space, by examining the local checkerboard wavelength defined by the distance between adjacent peaks. The local checkerboard wavelength is strongly correlated with gap size.

All of these results point toward the novel idea that the Fermi surface, generally thought of as an attribute of the entire crystal, can vary on a very local (nanometer) scale. This implies that bulk measurements that are affected by the Fermi surface are in fact averaging over the many Fermi surfaces of the nanoscale regions that make up the sample. The fact that the Fermi surface can vary on this length scale is discovery about fundamental solid-state physics, and one which has implications for interpretation of experimental results on the cuprates and on other inhomogeneous materials.

## 3.1 Measuring Fermi surface variations in an inhomogeneous superconductor

This section is almost identical to our paper in Nature Physics[2] and is reproduced with permission.

Particle-wave duality suggests we think of electrons as waves stretched across a sample, with wavevector k proportional to their momentum. Their arrangement in "k-space," and in particular the shape of the Fermi surface, where the highest energy electrons of the system reside, determine many material properties. Here we use a novel extension of Fourier transform scanning tunneling microscopy to probe the Fermi surface of the strongly inhomogeneous Bi-based cuprate superconductors. Surprisingly, we find that rather than being globally defined, the Fermi surface changes on nanometer length scales. Just as shifting tide lines expose variations of water height, changing Fermi surfaces indicate strong local doping variations. This discovery, unprecedented in any material, paves the way for an understanding of other inhomogeneous characteristics of the cuprates, like the pseudogap magnitude, and highlights a new approach to the study of nanoscale inhomogeneity in general.

That high temperature superconductors should exhibit nanoscale inhomogeneity is unsurprising. In correlated electron materials, Coulomb repulsion between electrons hinders the formation of a homogeneous Fermi liquid, and complex real space phase separation is ubiquitous[55]. Scanning tunneling microscopy (STM) measurements have revealed significant spectral variations in a number of cuprates including $Bi_2Sr_2CuO_{6+x}$ (Bi-2201)[41] and $Bi_2Sr_2CaCu_2O_{8+x}$ (Bi-2212)[18,56,57].

This intrinsic inhomogeneity poses challenges to the interpretation of bulk or spatially averaged measurements. For example, angle resolved photoemission spectroscopy (ARPES) is a powerful technique for studying k-space structure in the cuprates[49]. However, ARPES can only provide spatially-averaged results, and uniting these with the nanoscale disordered electronic structure measured by STM remains a formidable task.

Our approach to addressing this issue originates from discoveries by Fourier transform scanning tunneling microscopy (FT-STM), which has emerged as an important tool for studying the cuprates. These studies begin with the collection of a spectral survey, in which differential conductance spectra, proportional to local density of states (LDOS), are measured at a dense array of locations, creating a three dimensional dataset of LDOS as a function of energy and position in the plane. By Fourier transforming constant energy slices of these surveys, referred to as LDOS or conductance maps, FT-STM allows the study of two phenomena linked to the cuprate FS (Figure 32b). First, non-dispersive wavevectors of the checkerboard-like charge order observed in many cuprates[26-28,30] are likely connected to the FS-nesting wavevectors near the anti-nodal $(\pi,0)$ Brillouin zone boundary (e.g. arrow in Figure 32b)[58]. Second, dispersive quasiparticle interference (QPI) patterns[42,59,60] originate from elastic scattering of quasiparticles on the Fermi surface near the nodal (π, π) direction[43]. Taken together, these phenomena provide complementary information about the cuprate FS.
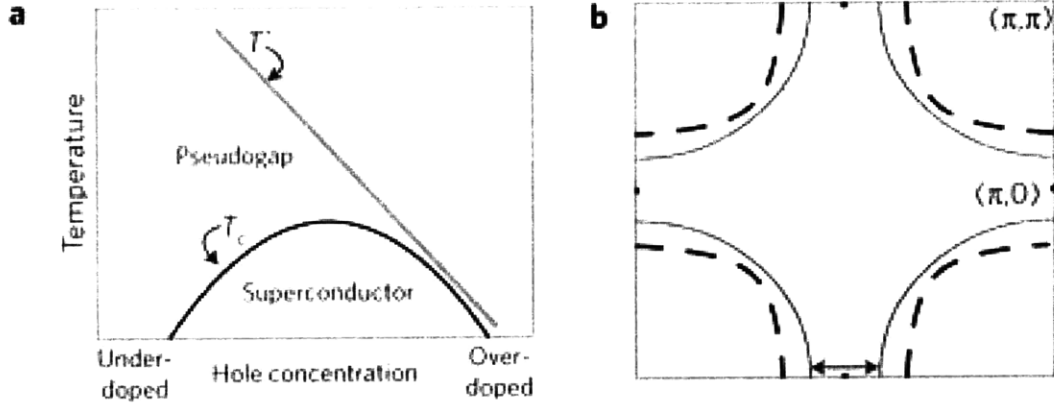
Figure 32. Generic phase diagram and Fermi surface.
a, A minimal generic phase diagram of the high-temperature superconductors shows a superconducting transition temperature T_c that is parabolic with doping, peaking at optimal doping, whereas the pseudogap temperature T^*—and the proportional pseudogap magnitude Δ_{PG}—decrease nearly linearly with doping. b, The hole-doped cuprate FS is typically seen as hole-like, closing around empty states centred at (π,π), rather than filled states centred at $(0, 0)$. Moving from optimally doped (solid line) to underdoped (dashed) materials, the hole pockets shrink. This increases the length of the nesting vector (arrow) near the antinode.

However, because these phenomena were previously characterized using Fourier transforms of large LDOS maps containing a wide range of energy gaps and spectra, previous FT-STM mapping of the FS was still spatially-averaged.[61] The atomic scale spatial resolution of STM was not exploited, so connections between FS geometry and local electronic structure went unexamined.

Here we introduce two new STM analysis techniques which allow extraction of a *local* FS. In studies of Bi-2201 and Bi-2212, we find that the cuprate FS varies at the nanometer scale, and that its local geometry correlates strongly with the size of the large, inhomogeneous energy gap that has been extensively studied by STM[18] and which we associate with the pseudogap[41].

We first investigate the spatial dependence of the anti-nodal FS using checkerboard charge order. Our recent study of Bi-2201 showed that the average checkerboard wavevector decreases with increased doping[58]. This trend, inconsistent with many proposed explanations of the checkerboard, matches the doping dependence of the anti-nodal FS-nesting wavevector (Figure 32b), and led us to conclude that the checkerboard is caused by a FS-nesting induced charge density wave. Here we continue the investigation of the three Bi-2201 dopings considered in our previous work, two underdoped with superconducting transitions at 25 K (UD25) and 32 K (UD32), and one optimally doped with $T_C = 35$ K (OP35). Although, following convention, we previously reported FT-measured, spatially averaged wavevectors, careful observation of the checkerboard pattern (Figure 33a) shows that the periodicity changes drastically with position.

One way of analyzing this variation is with a Voronoi diagram. After identifying local peaks of the checkerboard modulation (local maxima in the +10 mV conductance map, identified as red dots in Figure 33a), we divide the map into cells, each containing points closer to one checkerboard maximum than any other. The square root of the cell

size is a measure of the local checkerboard wavelength. We find that this local wavelength is highly correlated with the previously observed gap size inhomogeneity (Figure 33b,c), with a correlation coefficient of -0.4.
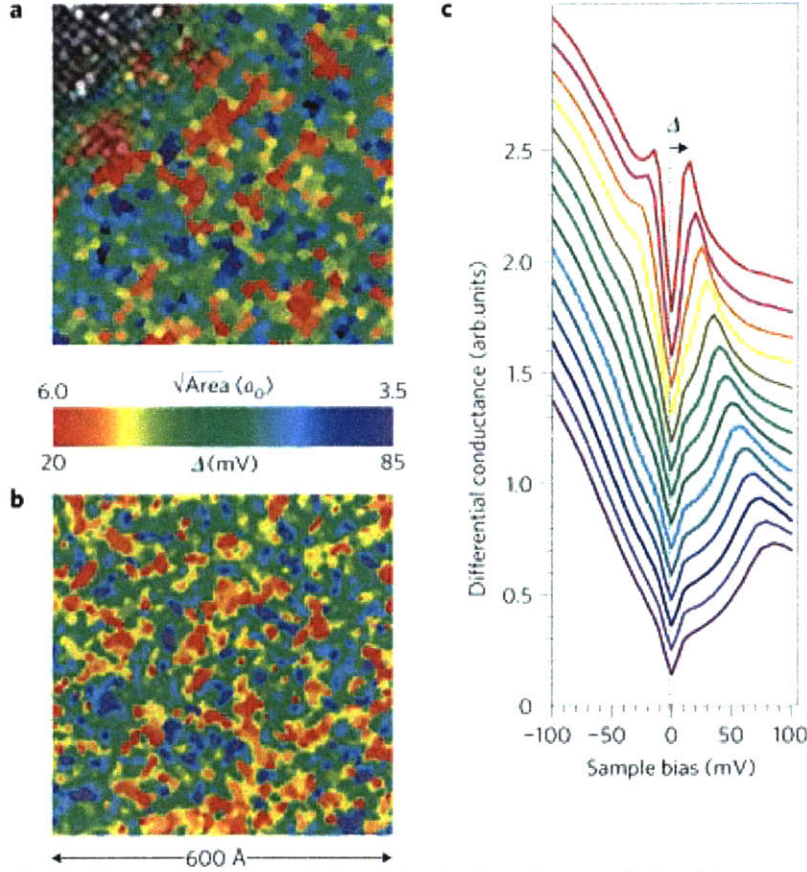
Figure 33. Real-space analysis of checkerboard-gap relationship.
a, Conductance map (energy E=+10 mV slice of a 400 pixel, 600 Å spectral survey) of T_c=32 K underdoped Bi-2201, showing a spatially varying checkerboard charge modulation (upper left). Voronoi cells, associated with checkerboard maxima (red dots) and coloured to indicate their area, enable determination of local wavelength. b, Traditional gap map of the same area showing well known variations of gap size Δ. c, Spectra from the survey (sorted, averaged and coloured by gap size, and shifted vertically for clarity) highlight the remarkable low-energy homogeneity in the presence of strong higher-energy inhomogeneity. Spectral survey parameters: I_{set}=400 pA, V_{sample}=-200 mV.

Another method of investigating this relationship between local checkerboard periodicity and gap size is to modify the traditional FT technique by first masking the LDOS map by gap size. This technique is illustrated in Figure 34. The LDOS map is set to zero everywhere outside a desired gap range and then Fourier transformed to reveal a gap dependent checkerboard wavevector. The result is qualitatively similar to the Fourier transform of the complete map, but the wavevector measured is due solely to the fraction of the sample within the selected range of gap magnitudes. Fourier transforms of different regions reveal different wavevectors (Figure 34b, c). Consistent with previously reported sample averages,[58] wavevectors increase with gap size (Figure 34d). We note this trend is not an artifact of mask geometry; rotating the masks, which preserves their geometry

while eliminating their relation to the gap map, eliminates the trend of figure 3d, instead simply yielding the sample average wavevector for all maps.

These two independent techniques not only demonstrate the inhomogeneity of the checkerboard wavelength, the likely cause of universally reported short checkerboard correlation lengths[58], but also reveal that the checkerboard wavevector and local gap size are strongly correlated. Between samples, average checkerboard wavevector decreases with increased doping[58], consistent with the decrease of the anti-nodal FS-nesting wavevector (Figure 32b). The tunneling measured gap size (scaling with pseudogap temperature T* of Figure 32a) also on average decreases with increased doping. Thus the positive correlation of local gap size and checkerboard wavevector is consistent with a picture in which local FS variations, driven by local doping variations, affect both. Notably, where gap sizes from different samples overlap, so do their checkerboard wavelengths (Figure 34d), indicating that checkerboard properties are truly set by local rather than sample average properties. We stress that this result is independent of the cause of the checkerboard, and relies only on our previously report of its doping dependence[58].
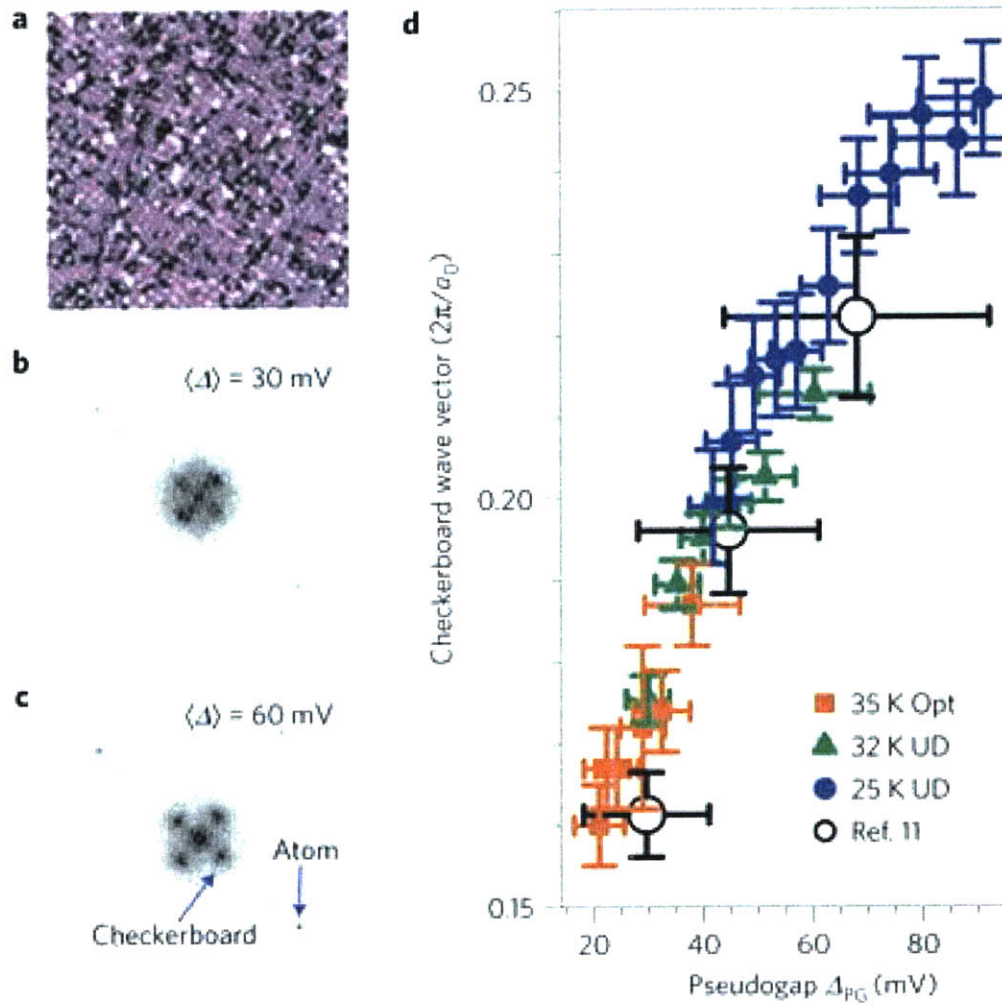
Figure 34. Gap dependence of the checkerboard wavelength.
a, Using the gap map of Figure 33b we mask the conductance map of Figure 33a, zeroing out (shading pink) data with gaps outside a desired range, here Δ=40–55 mV. b,c, Fourier transforms of the masked data (with $\langle \Delta \rangle$=30 mV (b) and $\langle \Delta \rangle$=60 mV (c)) show checkerboard wavevectors, whose length can be compared to the atomic periodicity, that shift with gap-masking range. d, Checkerboard wavevectors for this sample (green triangles) as well as optimally doped 35 K (orange square) and underdoped 25 K (blue circles) samples. Overlaid are large-area averages from our previous work[1]. Error bars indicate the standard deviation of the gap range used (horizontal) and the fast Fourier transform peak-fit accuracy (vertical). Gap ranges are non-uniform as they are selected to ensure roughly the same coverage in each mask.

In order to further investigate this idea we next turn to quasiparticle interference (QPI) studies of slightly overdoped (T_C = 89 K) Bi-2212. The idea behind QPI, pioneered by the Davis group[42,59,60] and Dung-Hai Lee,[43] is illustrated in Figure 35a. Interference patterns arising from quasiparticle scattering are dominated by wavevectors connecting k-space points of high density of states. For any given energy, eight such symmetric points exist, all on the FS. The well defined wavevectors (colored lines) of the resultant interference pattern can therefore be used to reconstruct the Fermi surface.

46

Just as in checkerboard studies, previous work on QPI has yielded spatially averaged results[42,59,60]. As above, we extend QPI analysis to yield local, gap dependent information. The interference wavevectors (circled in Figure 35b) found in Fourier transforms of gap masked conductance maps can be inverted to derive a FS[59], now associated with the gap range of the mask. Doing this for two different gap ranges, from 30 mV to 60 mV ($<\Delta> = 37$ mV), and 10 mV to 30 mV ($<\Delta> = 26$ mV), we find distinct shifts in the FS (Figure 35c). We extend this to the anti-node with checkerboard order, resolvable in Bi-2212 as non-dispersive order at energies above where the QPI signal weakens. Adding in nested anti-nodal FS segments (dashed lines) derived from checkerboard periodicity, we arrive at a nearly complete view of different local Fermi surfaces corresponding to different spatial locations, correlated spatially with different gap sizes. We also plot in Figure 35c rigid band tight binding Fermi surfaces[62] from two different dopings (p = 0.10 and 0.18 as calculated from the pocket area) very similar to the surfaces we derive.
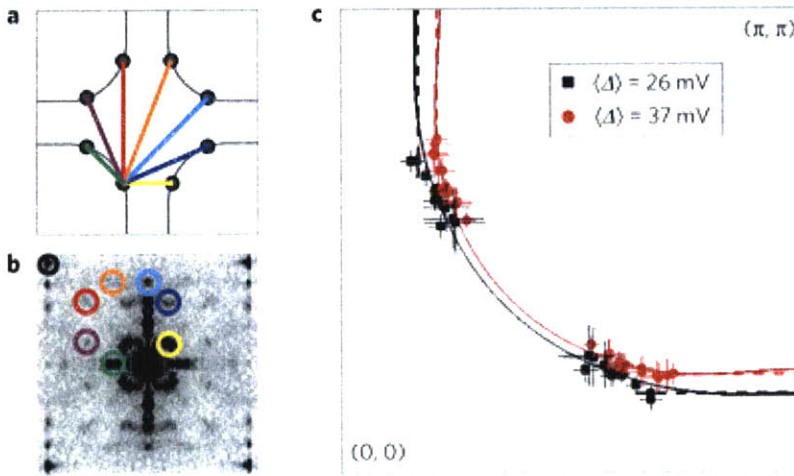
Figure 35. Local changes to quasiparticle interference patterns.
a, A schematic diagram of the FS (solid line) in the first Brillouin zone, showing symmetry, leading to an eightfold replication of any points at which the density of states peaks (for example circles). Scattering between quasiparticles at these points leads to a set of interference wavevectors (coloured lines), corresponding to peaks in interference maps such as b, a Fourier transform of a 600 Å, 400 pixel, E=12 mV conductance map of 89 K overdoped Bi-2212. The positions of these peaks (defined in terms of the atomic wavevector circled in black) uniquely define a position in k-space on the FS. Fitting interference peaks in a series of fast Fourier transform maps at various energies from two different masks of the same data leads to c, two different 'local FSs' (solid symbols with error bars indicating standard deviation for values obtained from different interference peaks). Dashed lines, obtained from checkerboard-determined nesting wavevectors, extend the determined FS to the antinode. Solid lines are FSs from a rigid-band, tight-binding model[62] at two different dopings, p=0.10 and 0.18.

Although **k**-space variation on nanometer length scales may at first glance seem shocking, upon further reflection this result is not entirely surprising. Raising or lowering a uniformly slanted sea floor near the shore (changing the amount of sea above the floor) changes the position of the shoreline. Analogously, raising or lowering local doping changes the local Fermi surface. McElroy et al. have even demonstrated that the locations of dopant oxygen atoms correlate with local gap size variations[16]. Interestingly,

the correlation McElroy *et al.* found was the opposite of what one might at first expect from a local doping picture. While oxygen dopants contribute holes and hence increase the global doping of the sample, they correlate with an *increased* local gap size, consistent with underdoping. This led the authors and others[63] to declare that variation in gap size is unlikely to be charge driven and instead propose variations in local pairing-potential.

The results we report here, however, cannot be explained by pairing-potential inhomogeneity. Instead, local doping variations appear most consistent with our results. Although McElroy *et al.* suggest that these variations cannot be explained by hole accumulation models, Zhou *et al.* claim that they have missed the oxygen atoms responsible for inhomogeneity[64]. Alternatively, local doping variations could be driven by dopant generated strain. This would also explain the correlation of gap variations with the strain-associated structural supermodulation in Bi-2212[65].

Regardless of the exact cause of these local doping variations, they can explain several previous results. Perhaps the clearest examples consist of recent STM results from the Yazdani group showing that the gap closing temperature varies spatially, scaling with local gap size,[57] and that both are correlated with higher temperature electronic structure[66]. Those results are unsurprising given the local Fermi surface variations we report here.

Considering the nature of the Fermi surface variations in detail, we find that the locally determined Fermi surfaces converge near the nodes while they are strongly inhomogeneous in the anti-nodes (Figure 35c). This could explain the ARPES-measured dichotomy of coherent nodal / incoherent anti-nodal quasiparticle excitations found in a variety of cuprates.[49,67] This differentiation is strongest in underdoped samples which could also arise from the inhomogeneity we report here. ARPES sums signal from differently doped regions; as more highly doped regions yield higher signal, ARPES will overemphasize them. Coupled with the observation that the width of the gap (and hence doping) distribution scales with mean gap size[68], and is thus smaller in overdoped than underdoped samples, inhomogeneity should have a stronger effect on ARPES measurements in underdoped than in overdoped samples. This effect is particularly apparent in Bi-2201, which is more inhomogeneous than Bi-2212.[41]

Despite the success of this interpretation, some outstanding questions remain. The model curves[62] of Figure 35c suggest that the effective band energy may shift by as much as 20 mV between different regions of the sample. This shift would lead to strong scattering, even in the nodal direction. However, aside from the reasonable match to our extracted Fermi surfaces, there is no reason to believe that this global average-extracted rigid band model should completely describe the local Fermi surfaces. For example, our extracted Fermi surfaces appear closer in the nodal region than the model surfaces.

Another question concerns a homogeneous gap we have reported.[41] The large, inhomogeneous gap discussed throughout this paper is probably more accurately termed the pseudogap, while we identified as the superconducting gap a second, relatively homogeneous smaller gap which opens at T_C. One might imagine that superconductivity, as characterized by size of the superconducting gap, should be as strongly affected by inhomogeneous local doping as the pseudogap. This is not what we have observed[41]. One explanation is that doping dependence differences make inhomogeneity affect the pseudogap more than the superconducting gap (the pseudogap, scaling with T*, changes

more than the superconducting gap, scaling with T_C). Another explanation may lie in their momentum space distribution. Raman spectroscopy[50] and ARPES[51,69] results indicate that the superconducting gap is most strongly associated with near-nodal states, while the pseudogap arises near the anti-nodes. As noted above, the nodal region is significantly more homogeneous than the antinodal, and hence could lead to more homogeneous superconducting than pseudogap properties.

This interpretation also points towards an explanation of bulk measurement results. Although several are suggestive of nanoscale inhomogeneity[18], including neutron measurements of the magnetic resonance peak width[70], thermodynamic measurements appear inconsistent with strong inhomogeneity[71]. These measurements, however, are most sensitive to the nature of the *superconducting* gap and the low energy density of states, both of which appear homogeneous. Undoubtedly these homogeneous properties relate to the homogeneity of the near nodal Fermi surface. Nonetheless, they are remarkable given the strong inhomogeneity we report here.

Inhomogeneity of doping or charge is common in many materials, and leads naturally to the idea of nanoscale Fermi surface variation. This work is, to our knowledge, the first attempt to characterize these variations, and raises the question of whether a Fermi surface, typically thought of as a bulk property, can be meaningfully defined inside nanometer sized domains. Although our experimental results appear consistent with this picture, further experimental and theoretical work are needed to determine at what point a k-space description such as this stops being useful.

3.11 Measuring Fermi surface variations in an inhomogeneous superconductor: supplement ***

This section is almost equivalent to the online supplement of the local Fermi surface paper discussed in the previous section.[2]

In this work we use the technique of Fourier transforming masked conductance maps to extract gap dependence of both the checkerboard wavelength and quasiparticle interference patterns. In this supplement we address some possible concerns about the results derived with this novel technique.

A first question is whether the geometry of the masks themselves could be responsible for the derived wavevector shifts. As noted in the text, we can test for such a masking effect by rotating masks before applying them to the conductance map, preserving mask geometry while removing the correlation between masks and the gap map. If mask geometry is responsible for the observed variations, then these variations should also be observed in Fourier transforms of data masked with rotated masks. If not, then rotated masks should yield non-dispersing (sample average) results. We show results of this test applied to $\langle\Delta\rangle = 30$ mV and 60 mV masks of data from a 32 K UD sample in Figure 36. While properly masked data shows strong gap dependent dispersion, as shown previously in Figure 34b and c, rotated masks produce nearly indistinguishable transforms Figure 36g and Figure 36h.
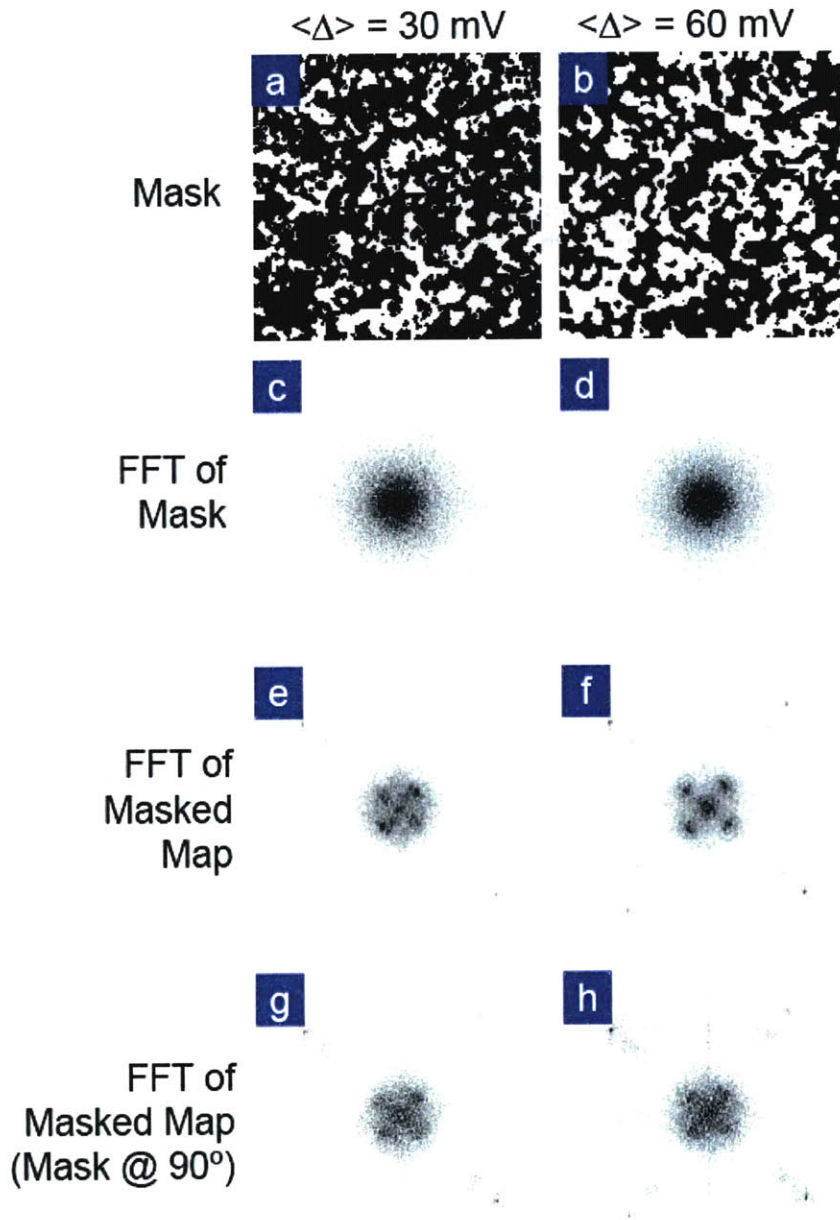
Figure 36. Testing the effects of mask geometry.
(a, b) Masks used for the 32K UD map of Figure 33 and Figure 34, where spectra taken in white areas show $\langle\Delta\rangle = 30$ mV and 60 mV respectively. (c, d) Fourier transforms (FTs) of those masks show no obvious structure at any particular wavelength, but instead highlight the low frequency inhomogeneity present in the sample. (e, f) Applying these masks to the map (by setting data in black regions to zero) and taking an FT yields the results of Figure 34b and c, reproduced here. (g, h) If the masks are first rotated 90°, breaking the correlation between mask and gap, the resultant FTs are similar to each other and the sample average.

Thus we conclude that map geometry is not responsible for the gap dependent wavevectors we report here, in either the checkerboard or quasiparticle interference results. Next, we test whether map geometry plays a role in the width of the Fourier peaks. We simulate an ideal (monochromatic) checkerboard, and mask and Fourier transform it with the 60 mV mask of Figure 36b. While the Fourier transform (FT) of the unmasked simulation shows four very sharp peaks (Figure 37b), that of the masked simulation (Figure 37d), shows broadened peaks, with width comparable to that of the data itself (Figure 37f), with a caveat. Line cuts through the peaks (Figure 37i) show that the masked simulation results (black squares) closely resemble the data (red squares), with the presence of an additional superimposed sharp peak. This discrepancy is due to the difference in correlation lengths of simulation and data. Measurement of domain sizes in gap maps show that domains typically have a diameter of 30 Å to 40 Å, or about $8a_0$ to $10a_0$. Perhaps surprisingly, this domain size seems independent of gap size and doping, and is the same in Bi-2201 and Bi-2212. Their size places a natural limit on the correlation length of the observed checkerboard pattern, which translates into a finite peak width, as shown in Figure 37i. Although the mask reflects this domain size, and hence leads to the same low amplitude shape in the simulated results, because the simulation is coherent it yields a sharp central peak, with width limited by the overall map size (600 Å). The effect of 30 Å domains in the data may be further compared to masking the simulation with a single 30 Å diameter circle. Although the amplitude of the transform is smaller, due to the smaller area being transformed, the width is comparable.
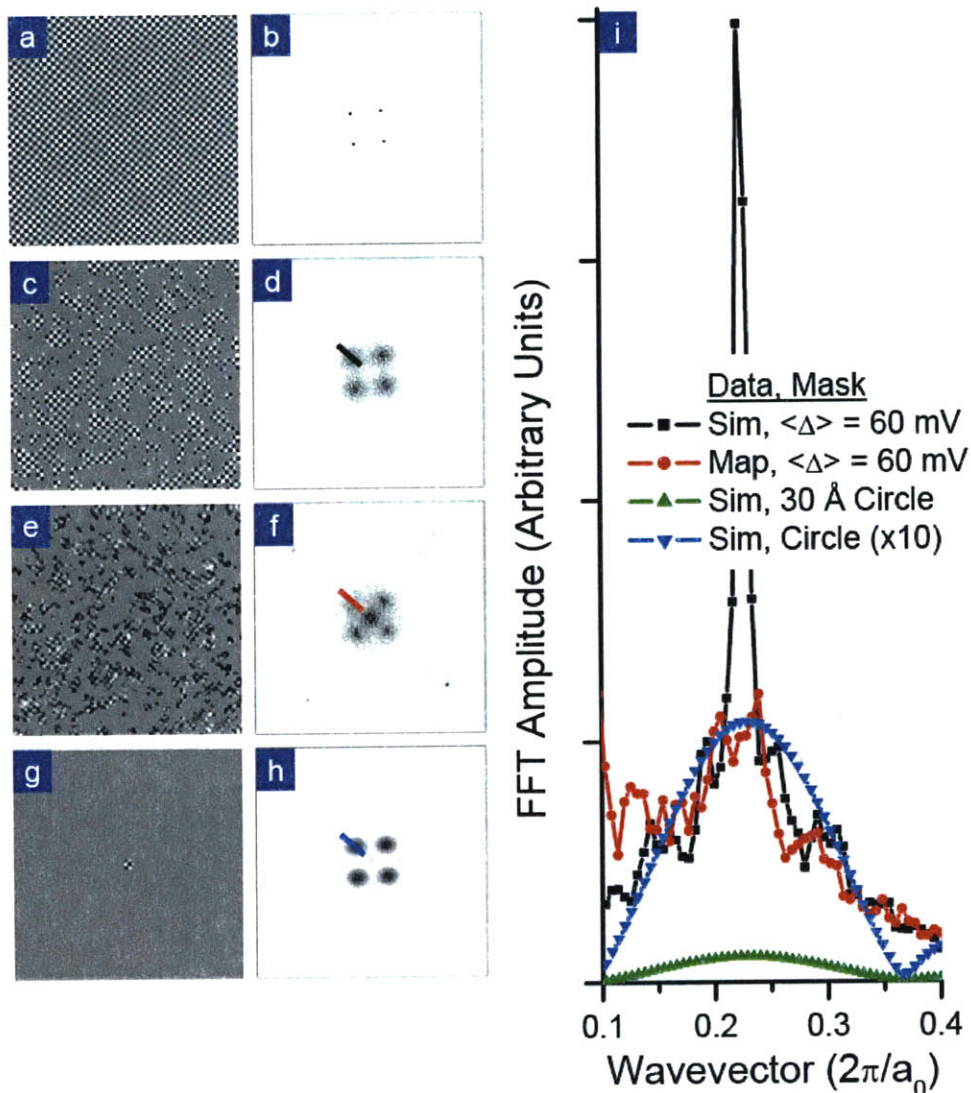
Figure 37. Mask geometry and peak width.
(a) A simulated checkerboard map, with a $4.7a_0$ wavelength (corresponding to the 0.213 $(2\pi/a_0)$ wavevector found for the $<\Delta> = 60$ mV masked 32K UD data). The map is 400 pixels over 600 Å, to match the data of Figure 33a. (b) The Fourier transform of this simulation shows 4 narrow peaks, as expected. (c, d) Masking the simulation with the $<\Delta> = 60$ mV mask of Figure 36b broadens the peaks, similar to the peaks in the data (e, f). (g, h) A single 30 Å diameter circle masking the simulation yields a similar width, although the amplitude is reduced and hence (h) is multiplied by 10 before being shown in the same color scale as (b, d, f). (i) Line cuts through the Fourier peaks (as shown by the short lines on d, f, and h) show the similar widths of data and simulation, due to the size of the gap domains and hence mask features.

The importance of the correlation length of the underlying (unmasked) data may be observed in Figure 38, where we show the effects of simulated phase disorder in our ideal checkerboard. While the FT of the ideal checkerboard shows a sharp central peak (black curve), as we introduce disorder by randomizing the phase in adjacent domains, the reduced correlation length causes the amplitude of the central peak to decrease as it broadens. Simulated phase disorder on a 30 Å length scale (cyan) effectively reproduces the data (red).
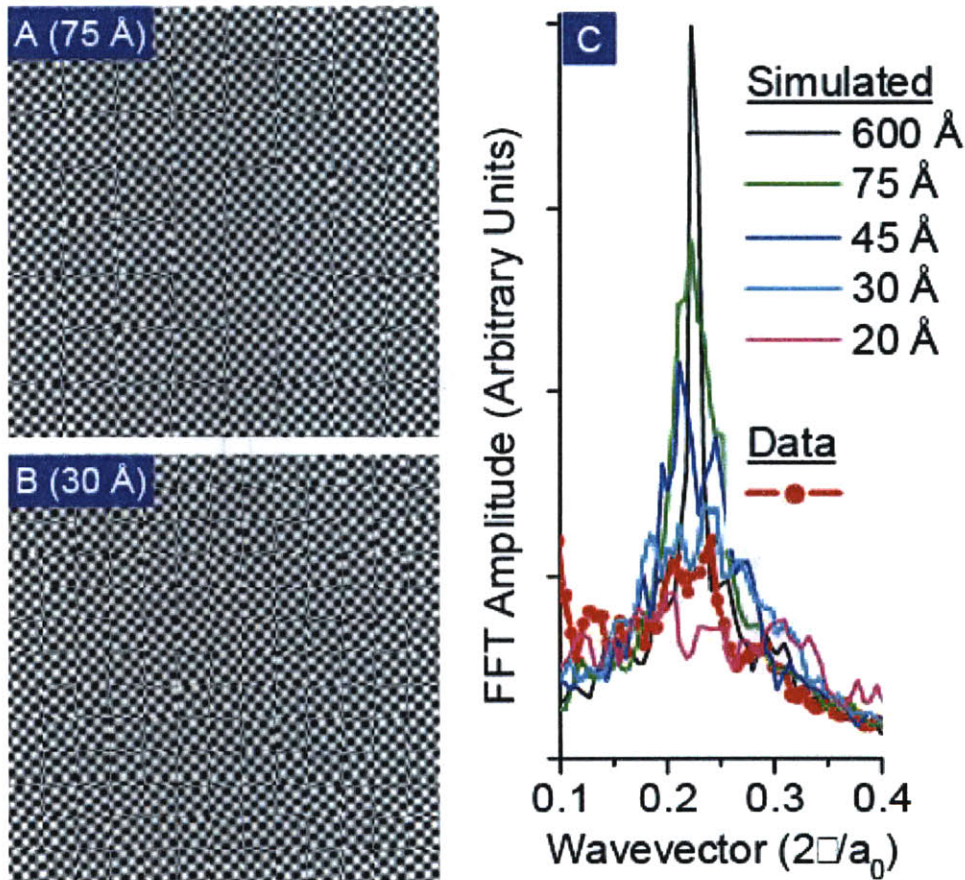
Figure 38. Correlation length effects.
(a,b) Simulated checkerboard maps with the same parameters of Figure 37, with the addition of phase disorder with 75 Å and 30 Å domains respectively. (c) Line cuts through Fourier transforms of maps such as a & b, masked and analyzed as in Figure 37, demonstrate the importance of the correlation length of the checkerboard in determining the amplitude and width of the central peak. The use of (b) 30 Å domains (cyan) effectively simulates the data (red).

In short, the peak width is not an artifact of map geometry, but rather reflects the inherent domain size and hence limited correlation length of gap dependent periodic modulations, such as the checkerboard and quasiparticle interference patterns. This has the related benefit that the exact mask used does not affect the gap size-wavevector relation we here report, as long as the mask captures the gap domains of interest. We

54

choose to make our masks cover a fixed fraction of the field of view, but what fraction is used plays no measureable role in the results.
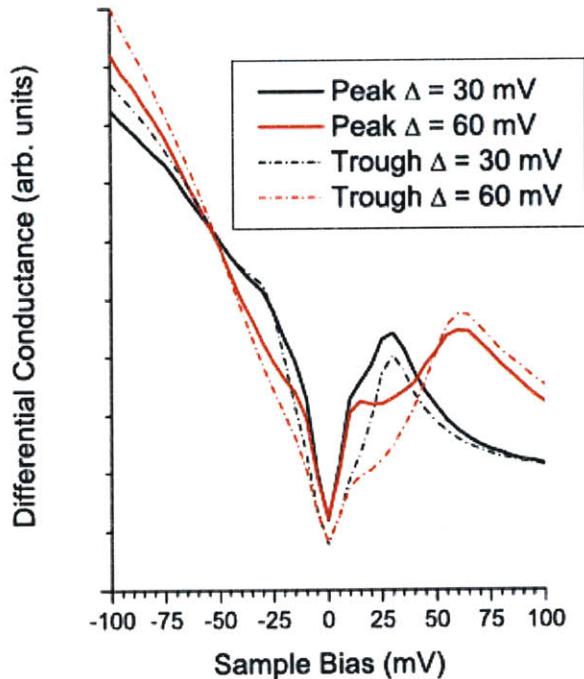
Figure 39. Position and gap dependent conductance.
Using the 32 K UD spectral survey analyzed throughout this paper, data is segregated by gap size as well as by whether it lies on a peak (the pixel lying at a checkerboard conductance maximum) or in a trough (the pixel wide boundary region between the Voronoi cells shown in Figure 33a). The average of such spectra for two gap sizes, Δ = 30 mV (black) and 60 mV (red), vary much more significantly with position, that is between peak (solid) and trough (dashed), than with gap size.

Finally, because of the clear relationship between gap magnitude and checkerboard periodicity, one might ask whether conductance variations associated with gap inhomogeneity could actually create the checkerboard modulation, or at least perturb its apparent wavelength. As we show in Figure 33c, there are significant conductance variations associated with gap inhomogeneity. Their position dependence, however, is quite interesting, as we show in Figure 39. Here we calculate the average conductance for four different types of regions in the sample, namely on and off of checkerboard peaks in Δ = 30 mV and 60 mV domains. Although low energy conductance is relatively homogeneous, the contrast at 10 mV, where the checkerboard is most clearly imaged, is clearly much higher between peaks and troughs (on and off the maxima) than it is between different gap regions. That is to say, conductance changes due to gap inhomogeneity are a small perturbation to those caused by the checkerboard modulation itself and hence cannot be concluded to cause the wavelength variations we report here. On a related note, although we use a typical STM normalization in reporting our data – fixing the integral of the differential conductance from 0 mV to some large voltage bias,

here -100 mV – the results presented here aren't particularly sensitive to this normalization. For example, if one instead chooses to fix the conductance in the wings (force the curves in Figure 39 to coincide at the left edge of the figure) the same dominance of checkerboard position over gap variation is still found.

References

[1] W. D. Wise, M. C. Boyer, Kamalesh Chatterjee et al., *Nat Phys* **4** (9), 696 (2008).

[2] W. D. Wise, Kamalesh Chatterjee, M. C. Boyer et al., *Nat Phys* **5** (3), 213 (2009).

[3] D. M. Eigler and E. K. Schweizer, *Nature* **344** (6266), 524 (1990).

[4] M.C. Boyer, Ph.D. Thesis, Massachusetts Institute of Technology, 2008.

[5] Kamalesh Chatterjee, M. C. Boyer, W. D. Wise et al., *Nature Phys.* **4** (2), 108 (2008).

[6] E. W. Hudson, Ph.D. Thesis, University of California, Berkeley, 1999.

[7] K. Chatterjee, Ph.D. Thesis., MIT, 2009.

[8] Leon N. Cooper, *Phys. Rev.* **104** (4), 1189 (1956).

[9] J. Bardeen, L. N. Cooper, and J. R. Schrieffer, *Phys. Rev.* **106** (1), 162 (1957).

[10] J. Bardeen, L. N. Cooper, and J. R. Schrieffer, *Phys. Rev.* **108** (5), 1175 (1957).

[11] J. E. Hoffman, Ph.D. Thesis, University of California, Berkeley, 2003.

[12] S. H. Pan, E. W. Hudson, and J. C. Davis, *App. Phys. Lett.* **73** (20), 2992 (1998).

[13] W. L. McMillan, *Phys. Rev.* **167** (2), 331 (1968).

[14] J. G. Bednorz and K. A. Müller, *Z. Phys. B* **64** (2), 189 (1986).

[15] P. Dai, B. C. Chakoumakos, G. F. Sun et al., *Physica C* **243** (3-4), 201 (1995).

[16] K. McElroy, Jinho Lee, J. A. Slezak et al., *Science* **309** (5737), 1048 (2005).

[17] S. H. Pan, J. P. O'Neal, R. L. Badzey et al., *Nature* **413** (6853), 282 (2001).

[18] K. M. Lang, V. Madhavan, J. E. Hoffman et al., *Nature* **415** (6870), 412 (2002).

[19] Patrick A. Lee, Naoto Nagaosa, and Xiao-Gang Wen, *Rev. Mod. Phys.* **78**, 17 (2006).

[20] C. E. Gough, M. S. Colclough, E. M. Forgan et al., *Nature* **326** (6116), 855 (1987).

[21] Hyekyung Won and Kazumi Maki, *Phys. Rev. B* **49** (2), 1397 (1994).

[22] H. Ding, M. R. Norman, J. C. Campuzano et al., *Phys. Rev. B* **54** (14), R9678 (1996).

[23] Ch Renner, B. Revaz, J. Y. Genoud et al., *Phys. Rev. Lett.* **80** (1), 149 (1998).

[24] M. R. Norman, H. Ding, M. Randeria et al., *Nature* **392** (6672), 157 (1998).

[25] A. Kanigel, M. R. Norman, M. Randeria et al., *Nature Phys.* **2** (7), 447 (2006).

[26] Michael Vershinin, Shashank Misra, S. Ono et al., *Science* **303**, 1995 (2004).

[27] K. McElroy, D. H. Lee, J. E. Hoffman et al., *Phys. Rev. Lett.* **94** (19), 197005 (2005).

[28] T. Hanaguri, C. Lupien, Y. Kohsaka et al., *Nature* **430** (7003), 1001 (2004).

[29] J. E. Hoffman, E. W. Hudson, K. M. Lang et al., *Science* **295** (5554), 466 (2002).

[30] C. Howald, H. Eisaki, N. Kaneko et al., *Phys. Rev. B* **67** (1), 014533 (2003).

[31] Y. Chen and C. S. Ting, *Phys. Rev. B* **65**, 180513 (2002); M. Franz, D. E. Sheehy, and Z. Tesanovic, *Phys. Rev. Lett.* **88**, 257005 (2002); Y. Zhang, E. Demler, and S. Sachdev, *Phys. Rev. B* **66**, 094501 (2002); J. X. Zhu, I. Martin, and A. R. Bishop, *Phys. Rev. Lett.* **89** (6), 067003 (2002).

[32] S. Sachdev and S. C. Zhang, *Science* **295** (5554), 452 (2002).

[33] S. A. Kivelson, I. P. Bindloss, E. Fradkin et al., *Rev. Mod. Phys.* **75**, 1201 (2003).

[34] D. Podolsky, E. Demler, K. Damle et al., *Phys. Rev. B* **67** (9), 094514 (2003).

[35] Han-Dong Chen, Oskar Vafek, Ali Yazdani et al., *Phys. Rev. Lett.* **93**, 187002 (2004).

[36] Z. Tesanovic, *Phys. Rev. Lett.* **93** (21), 217004 (2004).

[37] Jian-Xin Li, Chang-Qin Wu, and Dung-Hai Lee, *Phys. Rev. B* **74** (18), 184515 (2006).

[38] Kangjun Seo, Han-Dong Chen, and Jiangping Hu, *Phys. Rev. B* **76** (2), 020511 (2007).

[39] Kyle M. Shen, F. Ronning, D. H. Lu et al., *Science* **307**, 901 (2005).

[40] Takeshi Kondo, Tsunehiro Takeuchi, Uichiro Mizutani et al., *Phys. Rev. B* **72**, 024533 (2005).

[41] M. C. Boyer, W. D. Wise, Kamalesh Chatterjee et al., *Nature Phys.* **3** (11), 802 (2007).

[42] J. E. Hoffman, K. McElroy, D. H. Lee et al., *Science* **297** (5584), 1148 (2002).

[43] Qiang-Hua Wang and Dung-Hai Lee, *Phys. Rev. B* **67** (2), 020511 (2003).

[44] R. S. Markiewicz, S. Sahrakorpi, M. Lindroos et al., *Phys. Rev. B* **72**, 054519 (2005).

[45] U. Chatterjee, M. Shi, A. Kaminski et al., *Phys. Rev. Lett.* **96** (10), 107006 (2006).

[46] B. Lake, G. Aeppli, K. N. Clausen et al., *Science* **291** (5509), 1759 (2001).

[47] K. Yamada, C. H. Lee, K. Kurahashi et al., *Phys. Rev. B* **57** (10), 6165 (1998).

[48] W. Meevasana, N. J. C. Ingle, D. H. Lu et al., *Phys. Rev. Lett.* **96** (15), 157003 (2006).

[49] Andrea Damascelli, Zahid Hussain, and Zhi-Xun Shen, *Rev. Mod. Phys.* **75**, 473 (2003).

[50] M. Le Tacon, A. Sacuto, A. Georges et al., *Nature Phys.* **2**, 537 (2006).

[51] Takeshi Kondo, Tsunehiro Takeuchi, Adam Kaminski et al., *Phys. Rev. Lett.* **98** (26), 267004 (2007).

[52] W. S. Lee, I. M. Vishik, K. Tanaka et al., *Nature* **450** (7166), 81 (2007).

[53] Serban Smadici, Peter Abbamonte, Munetaka Taguchi et al., *Phys. Rev. B* **75** (7), 075104 (2007).

[54] P. Abbamonte, A. Rusydi, S. Smadici et al., *Nature Phys.* **1** (3), 155 (2005).

[55] E. Dagotto, *Science* **309** (5732), 257 (2005).

[56] C. Howald, P. Fournier, and A. Kapitulnik, *Phys. Rev. B* **64**, 100504 (2001).

[57] Kenjiro K. Gomes, Abhay N. Pasupathy, Aakash Pushp et al., *Nature* **447** (7144), 569 (2007).

[58] W. D. Wise, M. C. Boyer, Kamalesh Chatterjee et al., *Nature Phys.* **Advanced Online Publication** (2008).

[59] K. McElroy, R. W. Simmonds, J. E. Hoffman et al., *Nature* **422** (6932), 592 (2003).

[60] T. Hanaguri, Y. Kohsaka, J. C. Davis et al., *Nature Phys.* **3** (12), 865 (2007).

[61] Adrian Del Maestro, Bernd Rosenow, and Subir Sachdev, *Phys. Rev. B* **74** (2), 024520 (2006).

[62] M. R. Norman, M. Randeria, H. Ding et al., *Phys. Rev. B* **52** (1), 615 (1995).

[63] Tamara S. Nunner, Brian M. Andersen, Ashot Melikyan et al., *Phys. Rev. Lett.* **95** (17), 177003 (2005).

[64] Sen Zhou, Hong Ding, and Ziqiang Wang, *Phys. Rev. Lett.* **98** (7), 076401 (2007).

[65] J. A. Slezak, Jinho Lee, M. Wang et al., *PNAS* **105** (9), 3203 (2008).
[66] Abhay N. Pasupathy, Aakash Pushp, Kenjiro K. Gomes et al., *Science* **320** (5873), 196 (2008).
[67] X. J. Zhou, T. Yoshida, D. H. Lee et al., *Phys. Rev. Lett.* **92** (18), 187001 (2004).
[68] J. W. Alldredge, Jinho Lee, K. McElroy et al., *Nat Phys* **4** (4), 319 (2008).
[69] Kiyohisa Tanaka, W. S. Lee, D. H. Lu et al., *Science* **314** (5807), 1910 (2006).
[70] B. Fauque, Y. Sidis, L. Capogna et al., *Phys. Rev. B* **76** (21), 214512 (2007).
[71] J. W. Loram and J. L. Tallon, in *cond-mat* (2006), Vol. 0609, pp. 305.